



# Multiscale micromechanics modeling of plant fibers: upscaling of stiffness and elastic limits from cellulose nanofibrils to technical fibers

Markus Königsberger · Markus Lukacevic · Josef Füssl

Received: 23 February 2022 / Accepted: 28 December 2022 / Published online: 12 January 2023  
© The Author(s) 2023

**Abstract** The mechanical properties of natural fibers, as used to produce sustainable biocomposites, vary significantly—both among different plant species and also within a single species. All plants, however, share a common microstructural fingerprint. They are built up by only a handful of constituents, most importantly cellulose. Through continuum micromechanics multiscale modeling, the mechanical behavior of cellulose nanofibrils is herein upscaled to the technical fiber level, considering 26 different commonly used plants. Model-predicted stiffness and elastic limit bounds, respectively, frame published experimental ones. This validates the model and corroborates that plant-specific physicochemical properties, such as microfibril angle and cellulose content, govern the mechanical fiber performance.

**Keywords** Natural fibers · Biocomposite · Strength · Elasticity · Micro-mechanics

## 1 Introduction

Increasing environmental concerns have led to a renaissance of natural plant fibers. They are abundantly available in most regions of the world and have proven to be a sustainable and cost-effective alternative to synthetic fibers for the production of high-performance fiber-reinforced biocomposite materials, see Fig. 1d, usable across several engineering fields [1–6], e.g. for lightweight structural elements in the construction sector. Given the sheer amount of possible source materials (including fibers from different plants as well as different binders) and different fiber treatment and composite production technologies, which result in a very specific mechanical composite performance [5, 7–9], micromechanics-based modeling of the three-dimensional mechanical behavior is essential to characterize and optimize existing composites and engineer new ones. As a prerequisite for biocomposites modeling, a micromechanics-based description of the mechanical behavior of plant fibers used for biocomposite production is essential and is dealt with herein.

The mechanical properties of natural fibers vary significantly, ranging from axial moduli of only 10 GPa and axial tensile strengths of less than 100 MPa for coir or oil palm leaf fibers [10, 11] to moduli up to 100 GPa and strengths up to 1800 MPa for bast fibers such as flax or ramie [4, 12, 13], which is comparable to synthetic glass fibers. Even for a given

---

M. Königsberger · M. Lukacevic · J. Füssl  
Institute for Mechanics of Materials and Structures, TU  
Wien, Karlsplatz 13/202, 1040 Vienna, Austria

M. Königsberger (✉)  
BATiR Department, Université Libre de Bruxelles,  
CP194/04, 50 avenue F.D. Roosevelt, 1050 Brussels,  
Belgium  
e-mail: markus.koenigsberger@tuwien.ac.at



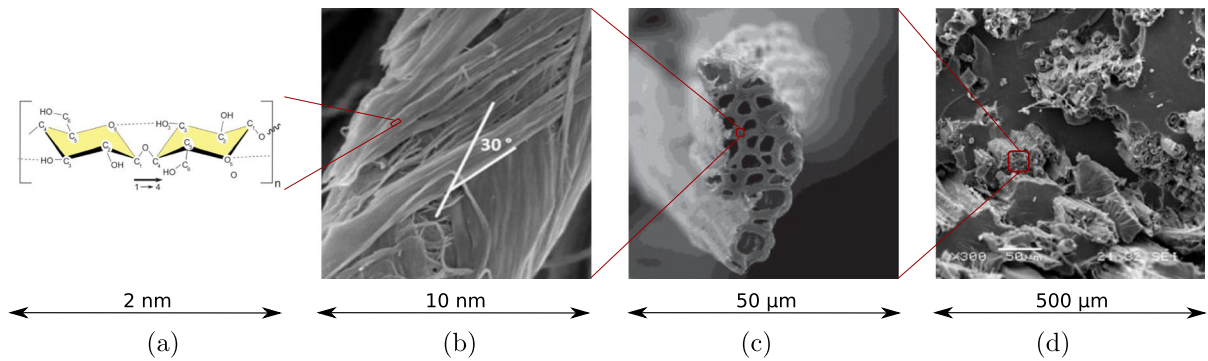


**Fig. 1** Multiscale structure of biocomposites: **a** physicochemical structure of cellulose chain [14], **b** SEM image of cellulose microfibril in bamboo fiber with microfibril angle of 30° [15],

**c** SEM image of jute fiber cross Sect. [10], **d** hemp oil-based biocomposite with jute fiber reinforcements [16]

fiber species, the mechanical fiber properties fluctuate, depending on geographical locations, maturity at harvest, location within the plant, growing conditions, processing methods, and potential treatments [2, 5, 6].

Despite the variety, all natural fibers share a common microstructural fingerprint [10], see Fig. 1a–c, which is shortly recalled next. Technical plant fibers typically consist of many fiber cells, formed by the central lumen, surrounded by the cell wall and connected together by the middle lamellae, see Fig. 1c. The cell wall, in turn, consists of a primary and several secondary layers, out of which the S2 layer is by far the thickest [17]. The S2 layer contains amorphous lignin and hemicellulose regions intermixed with cellulose microfibrils disposed in a right-hand spiral, see Fig. 1(b). The angle between the fiber axis and the microfibrils in the S2 layer, denoted as microfibril angle, is a key driver for the mechanical properties of the fiber [1]. The microfibrils themselves contain cellulose either in highly ordered arrangement forming smaller nanofibrils (crystalline cellulose) or disordered arrangement (amorphous cellulose) [14]. The excellent mechanical properties of plant fibers originate from the cellulose nanofibril which, at the molecular scale, is built up by a linear chain of anhydroglucose rings, linked together by covalent oxygen bonds and stabilized by hydrogen bonds [14], see Fig. 1a. The mechanical properties of cellulose nanofibrils themselves have been deciphered recently: the molecular dynamics-derived elastic modulus (in axial chain direction) amounts to roughly 170 GPa [18, 19], the axial tensile strength, in turn, quantified by sonication-induced fragmentation testing [20], amounts to roughly 2300 MPa.

The goal of this paper is to quantitatively link the nanoscale cellulose properties (170 GPa modulus, 2300 MPa strength) to the macroscopic properties of common plant fibers (10–100 GPa modulus, 100–1800 MPa strength). We explore whether both the reduction of the mechanical performance upon transition from the nanoscale to the macroscale as well as the differences in mechanical properties among the fibers from different plants result from plant-specific physicochemical parameters such as microfibril angle, cell wall thickness, and lumen size, as well as from plant-specific amounts and crystallinities of cellulose. As for the required scale transition, we rely on micromechanics-based multiscale modeling. Microstructure-based models for predicting mechanical properties of plant fibers have been developed for several decades. Hearle [21] modeled the plant cell walls as spiral springs. To model the different layers in the cell walls, laminate theory was frequently used [22–24]. More recently, continuum micromechanics multiscale models have been successfully applied to predict the (poro-)elastic stiffness [25–27] and elastic limits [28, 29] of clear-wood. Gangwar and co-workers [30, 31] extended the micromechanics model to predict the axial, shear, as well as bending behavior of whole plant culms, which was in good agreement with experimentally tested behavior of bamboo and oat stems. In this paper, we adopt and extend the continuum micromechanics multiscale representation of wood [25–27] towards the most common natural fibers. Thereby, we consider only the essential microstructural features, i.e. the elongated cylindrical shape of cellulose fibrils and lumen pores, the microfibril angle in the S2 layer, and the hierarchical

organization and interaction, as well as the contents of the microstructural constituents.

For model validation, 26 of the most common plant fibers, including fibers obtained from bast, grass, leaves, fruits, seeds, and straws are studied. As for the required model input regarding physicochemical fiber properties, we gather published experimental data, which reveals, much like the mechanical fiber properties, rather significant differences in between different literature sources, resulting in rather large intervals for each property reported in the literature. Notably, measured microscopic physicochemical and macroscopic mechanical fiber properties typically stem from different experimental campaigns. This renders the comparison of model-predicted mechanical properties, which rest on the physicochemical input properties, to experimentally determined counterparts, obtained from single-fiber testing, rather difficult. To overcome this challenge and to avoid any bias, we collect large databases for both the microscopic physicochemical and macroscopic mechanical fiber properties. The micromechanics model is then evaluated for the collected physicochemical interval, whereby we combine (i) unfavorable features such as a small cellulose contents with a large microfibril angles and with a large lumen porosities, to obtain a lower bound for the predicted stiffness and strength; and (ii) favorable features to obtain an upper bound. This results in predicted intervals of macroscopic mechanical fiber properties, which can be justly compared to the corresponding experimentally measured intervals, for all 26 studied fibers. This way, despite all experimental challenges and scattered fiber behavior, the model performance can be assessed and plant-specific differences can be discussed appropriately.

## 2 Multiscale micromechanics modeling

### 2.1 Micromechanics representation of plant-based biocomposites

The complex microstructure of plant fibers is taken into account by several linked representative volume elements (RVEs), describing the material morphology at different length scales. The material phases defining each RVE are represented by homogeneous subdomains, whose physical quantities (such as density,

stiffness) are intrinsic and known. Notably, RVEs have to satisfy the scale separation criterion [32], reading as

$$d \ll \ell \ll \mathcal{L}. \quad (1)$$

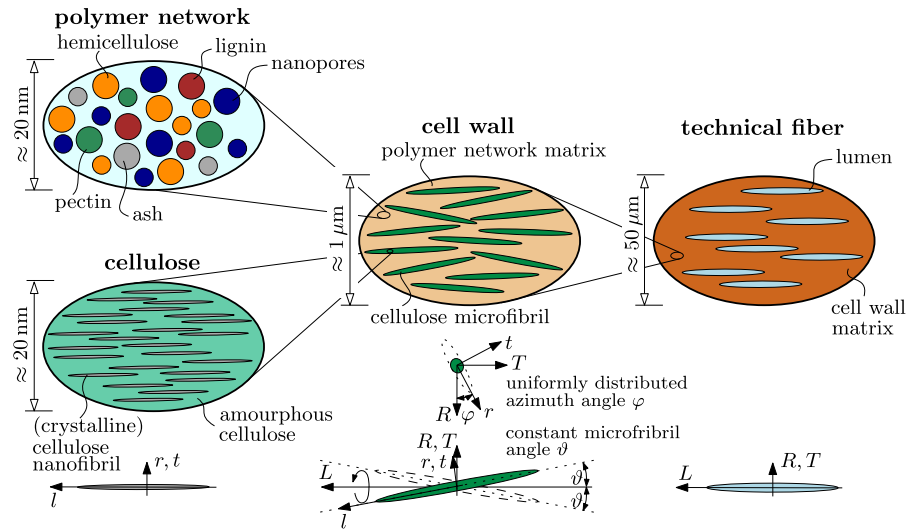
Inequalities (1) imply that the RVE's characteristic size  $\ell$  is considerably larger than the characteristic size  $d$  of the material phases contained inside the RVE and, at the same time,  $\ell$  is considerably smaller than characteristic size  $\mathcal{L}$  of the structure containing the RVE. In a multiscale setting of RVEs,  $\mathcal{L}$  takes the role of a phase which is further resolved at a smaller observation scale, i.e. RVE 1 has to be significantly smaller than the phase (inside a larger RVE 2) which is built up by RVE 1.

We model plant fibers by means of four RVEs distributed across three scales of observation, as described next. At the scale of several nanometers we adopt the representation of wood, originally developed to predict the elastic properties [25, 26], later extended towards strength predictions [28, 33], poromechanics [27, 29] and towards plant culms [30, 31]. In more detail, an RVE referred to as “polymer network” is considered to consist of five spherical phases: hemicellulose, lignin, pectin, nanopores [initially filled with extractives (including waxes, oils, fats), and potentially emptied during fiber processing], and ashes (inorganic parts), see Fig. 2. At the same length scale, we introduce an that the “cellulose” RVE which is built up by unidirectional crystalline cellulose nanofibril phases, modeled as infinitely long aligned cylinders embedded in a matrix of amorphous cellulose.

At the scale of a single micron, we consider the “cell wall” RVE to consist of infinitely long cylindrical cellulose microfibrils embedded in a matrix of polymer network. The crystalline cellulose nanofibrils are aligned with the cellulose microfibril orientation with coordinate base  $r, t, l$ , whereby  $l$  is the longitudinal direction along the fibril axis. Cellulose microfibrils and plant fibers (with coordinate base  $R, T, L$ ), however, are typically not aligned. To account for the microfibril orientation, found in the central S2 layer of plant cell walls [34], the microfibrils are considered to be rotated by a constant microfibril angle  $\theta$ , defined as the angle between the microfibril orientation  $l$  and the longitudinal plant fiber direction  $L$ , see the orientations indicated below the



**Fig. 2** Multiscale micromechanics representation of plant fibers by means of four scale-separated RVEs across three scales of observation, and orientation of phases with respect to local microfibril-related base frame  $e_r, e_t, e_l$  or the global base frame  $e_R, e_T, e_L$ ; 2D sketches refer to 3D RVEs



RVEs in Fig. 2. The microfibril orientation with respect to the  $R - T$ -plane is considered to be uniformly distributed. Finally, at the scale of several tens of microns, we consider the RVE of the “technical fiber”, multi-cellular structures with several individual tracheids bound to a fiber bundle [35], which are modeled by a cell wall matrix phase with embedded infinitely long cylindrical lumen porosity aligned with the longitudinal fiber direction  $L$ .

### 2.2 Stiffness homogenization

We herein aim at stiffness upscaling, i.e. at homogenizing the stiffness of the micro- or nanoscopic phases to predict, based on the envisioned micromechanics multiscale representation of Fig. 2, the stiffness of the technical fibers from different plants. All phases are considered to be linear elastic and also intrinsic, i.e. they do not vary from one plant to another. Crystalline  $I\beta$  cellulose, the dominant polymorph for plants [14], has been studied experimentally by means of X-ray scattering [36–38] and atomic force microscopy [39], as well as numerically by means of molecular simulations [18, 40–42]. The molecular structure of cellulose is characterized by strong covalent bonds in longitudinal  $l$ -direction (local base) but rather weak bonding by Van der Waals forces in the other directions, resulting in a large longitudinal but rather small radial/tangential stiffness [42]. Reported elastic moduli in longitudinal direction range from 110 GPa [41] to 220 GPa [38], see also

the review of Moon et al. [14]. We rely on the well-established simulation results of Tashiro and Kobayashi [18], reporting a modulus of 167.8 GPa, a value close to the center of the reported interval. The corresponding stiffness tensor  $\mathbb{C}_{NF}$  is approximated to be transversally isotropic, with stiffness tensor components, referring to the local microfibril base system  $e_r, e_t, e_l$ , reading as [25] [unit: GPa]

$$\mathbb{C}_{NF} = \begin{bmatrix} 34.86 & 0 & 0 & 0 & 0 & 0 \\ 0 & 34.86 & 0 & 0 & 0 & 0 \\ 0 & 0 & 167.8 & 0 & 0 & 0 \\ 0 & 0 & 0 & 11.61 & 0 & 0 \\ 0 & 0 & 0 & 0 & 11.61 & 0 \\ 0 & 0 & 0 & 0 & 0 & 34.86 \end{bmatrix} \begin{matrix} e_r \\ e_t \\ e_l \end{matrix} \quad (2)$$

whereby Kelvin-Mandel tensor notation [43] is used. The remaining phases are considered to be isotropic with phase stiffness tensors  $\mathbb{C}_i$  reading as

$$\mathbb{C}_i = 3k_i \mathbb{1}_{vol} + 2\mu_i \mathbb{1}_{dev} \quad (3)$$

where  $k_i$  and  $\mu_i$  denote the phase-specific bulk and shear moduli, and are obtained from experiments or molecular models, as summarized in Table 1, and with  $\mathbb{1}_{vol}$  and  $\mathbb{1}_{dev}$  as volumetric and deviatoric parts of the fourth order unity tensor.

Considering (i) linear constitutive relations  $\sigma_i = \mathbb{C}_i : \varepsilon_i$  with  $\sigma_i$  and  $\varepsilon_i$  as average phase stresses and strains, (ii) linearized strain-displacement relations,



**Table 1** Densities  $\rho_i$ , as well as bulk moduli  $k_i$  and shear moduli  $\mu_i$  of phases; properties refer to dry or nearly dry matter

Phase	$i$	$\rho_i$ [g/cm <sup>3</sup> ]	References	$k_i$ [GPa]	$\mu_i$ [GPa]	References
cellulose nanofibril	NF	1.59	[44]	anisotropic, see Eq.(2)		[18]
amorphous cellulose <sup>o</sup>	amcel	1.50	[45]	6.22	2.07	[42]
hemicellulose <sup>o</sup>	hemcel	1.46	[46]	8.08	3.73	[46, 47]
lignin	lig	1.27	[46]	5.00	2.31	[46, 48]
pectin*	pec	1.53	[49]	1	0.4	
nanopores (extractives)	npor	0.9	[25]	0	0	
ash <sup>†</sup>	ash	2.20	[50]	36.3	30.9	[50]
lumen pores (air-filled)	lum	0		0	0	

<sup>o</sup>Poisson's ratio assumed to be 0.35 [25]

\*elastic properties assumed

<sup>†</sup>properties of amorphous silica (silica glass) are considered representative

and (iii) equilibrium within an RVE containing  $N$  perfectly bonded phases, as well as homogeneous boundary conditions, implies a linear strain concentration relation from macrostrains  $\mathbf{E}$  down to microstrains  $\mathbf{\varepsilon}_i$ , reading as [32, 51]

$$\mathbf{\varepsilon}_i = \mathbb{A}_i : \mathbf{E} \quad \forall i \in N, \quad (4)$$

and thus a linear stiffness homogenization rule [51]

$$\mathbb{C}_{\text{hom}} = \sum_{i=1}^N f_i \mathbb{C}_i : \mathbb{A}_i \quad (5)$$

with  $\mathbb{A}_i$  as the (fourth-order) phase strain concentration tensor and  $f_i$  as the phase volume fraction (satisfying  $\sum_{i=1}^N f_i = 1$ ). Estimates for  $\mathbb{A}_i$  in continuum micromechanics, are obtained by introducing  $N$  Eshelby-type matrix-inclusion problems [52], such that the inclusion in one Eshelby problem represents one spheroidal phase of the RVE. They read as [32]

$$\mathbb{A}_i = \mathbb{A}_i^0 : \left( \sum_{j=1}^N f_j \mathbb{A}_j^0 \right)^{-1}, \quad (6)$$

with auxiliary concentration tensors  $\mathbb{A}_i^0$  reading as

$$\mathbb{A}_i^0 = [\mathbb{I} + \mathbb{P}_i : (\mathbb{C}_i - \mathbb{C}_0)]^{-1}, \quad (7)$$

whereby  $\mathbb{I}$  is the (fourth-order) identity,  $\mathbb{P}_i$  is the (fourth-order) Hill tensor accounting for the inclusion shape (see A), and  $\mathbb{C}_0$  is the stiffness of the infinite matrix in the Eshelby problem and is chosen based on the mode of interaction between the phases inside the RVE.

Stiffness homogenization according to Eqs. (5–7) is applied to the RVEs depicted in Fig. 2, starting at the smallest observation scale. The homogenized stiffness of the polymer network  $\mathbb{C}_{\text{pn}}$  follows from specialization of homogenization Eqs. (5–7) for  $N = 5$  spherical and isotropic phases for mutual interactions between all phases considered by the self-consistent scheme [53, 54] as

$$\mathbb{C}_{\text{pn}} = \left[ \sum_i f_i^{\text{pn}} \mathbb{C}_i : \left[ \mathbb{I} + \mathbb{P}_{\text{sph}}^{\text{pn}} : (\mathbb{C}_i - \mathbb{C}_{\text{pn}}) \right]^{-1} \right] : \left[ \sum_i f_i^{\text{pn}} \left[ \mathbb{I} + \mathbb{P}_{\text{sph}}^{\text{pn}} : (\mathbb{C}_i - \mathbb{C}_{\text{pn}}) \right]^{-1} \right]^{-1} \quad (8)$$

with  $i \in \{\text{hemcel}, \text{lig}, \text{pec}, \text{wax}, \text{ash}\}$  and  $\mathbb{P}_{\text{sph}}^{\text{pn}}$  as the Hill tensor of spherical phases in an infinite matrix of polymer network, see A. The homogenized stiffness of the cellulose microfibril  $\mathbb{C}_{\text{MF}}$  follows from specialization of homogenization Eqs. (5–7) for  $N = 2$  phases and for the envisioned matrix-inclusion morphology modeled by the Mori-Tanaka homogenization scheme [55, 56] as

$$\mathbb{C}_{\text{MF}} = \left( f_{\text{amcel}}^{\text{cel}} \mathbb{C}_{\text{amcel}} + f_{\text{NF}}^{\text{cel}} \mathbb{C}_{\text{NF}} : \mathbb{A}_{\text{NF}}^0 \right) : \left( f_{\text{amcel}}^{\text{cel}} \mathbb{I} + f_{\text{NF}}^{\text{cel}} \mathbb{A}_{\text{NF}}^0 \right)^{-1} \quad (9)$$

with



$$\mathbb{A}_{\text{NF}}^0 = \left[ \mathbb{I} + \mathbb{P}_{\text{cyl}}^{\text{amcel}} : (\mathbb{C}_{\text{NF}} - \mathbb{C}_{\text{amcel}}) \right]^{-1}, \quad (10)$$

and with Hill tensor components of  $\mathbb{P}_{\text{cyl}}^{\text{pn}}$  given in A. The homogenized stiffness of the cell wall  $\mathbb{C}_{\text{cw}}$  follows from specialization of homogenization Eqs. (5–7) for  $N = 2$  phases, and again for the envisioned matrix-inclusion morphology modeled by the Mori-Tanaka homogenization scheme [55, 56]. Given the microfibril orientation with constant microfibril angle  $\vartheta \geq 0$  but uniform orientation along the azimuth  $\varphi$ , integration along the circumference is required, yielding

$$\mathbb{C}_{\text{cw}} = \left[ f_{\text{pn}}^{\text{cw}} \mathbb{C}_{\text{pn}} + \frac{f_{\text{MF}}^{\text{cw}}}{2\pi} \int_0^{2\pi} \mathbb{C}_{\text{MF}} : \mathbb{A}_{\text{MF}}^0(\varphi) d\varphi \right] : \left[ f_{\text{pn}}^{\text{cw}} \mathbb{I} + \frac{f_{\text{MF}}^{\text{cw}}}{2\pi} \int_0^{2\pi} \mathbb{C}_{\text{MF}} : \mathbb{A}_{\text{MF}}^0(\varphi) d\varphi \right]^{-1} \quad (11)$$

with

$$\mathbb{A}_{\text{MF}}^0(\varphi) = \left[ \mathbb{I} + \mathbb{P}_{\text{cyl}}^{\text{pn}}(\varphi) : (\mathbb{C}_{\text{MF}} - \mathbb{C}_{\text{pn}}) \right]^{-1}, \quad (12)$$

with Hill tensor components of  $\mathbb{P}_{\text{cyl}}^{\text{pn}}$  given in A. Notably, any asymmetries related to Mori-Tanaka homogenization with anisotropic phases [57] are symmetrized [58]. Finally, the homogenized stiffness of the technical fiber  $\mathbb{C}_{\text{fib}}$  follows from specialization of homogenization Eqs. (5–7) for  $N = 2$  phases and again for the envisioned matrix-inclusion morphology modeled by the Mori-Tanaka homogenization scheme [55, 56] as

$$\mathbb{C}_{\text{fib}} = f_{\text{cw}}^{\text{fib}} \mathbb{C}_{\text{cw}} : \left[ f_{\text{cw}}^{\text{cel}} \mathbb{I} + f_{\text{lum}}^{\text{cel}} \left( \mathbb{I} - \mathbb{P}_{\text{cyl}}^{\text{cw}} : \mathbb{C}_{\text{cw}} \right)^{-1} \right]^{-1} \quad (13)$$

with Hill tensor components of  $\mathbb{P}_{\text{cyl}}^{\text{cw}}$  given in A. The sought axial fiber modulus  $E_{\text{fib}} = 1/D_{\text{fib,LLLL}}$ , with  $\mathbb{D}_{\text{fib}} = \mathbb{C}_{\text{fib}}^{-1}$  as the fiber compliance tensor.

### 2.3 Elastic limit homogenization

Cellulose failure is considered to be responsible for failure of natural fibers. Experimental insights into cellulose failure is therefore discussed first. Access to the tensile failure properties of cellulose fibrils is currently limited to sonication-induced fragmentation testing from Saito et al. [20] and Lee et al. [59]. Native cellulose nanofibrils were isolated by means of TEMPO-mediated oxidation, and the suspensions were subsequently subjected to hydrodynamic stresses through sonication-induced cavitation, yielding fibril fragmentation. After prolonged sonication treatment, remaining fibrils exhibit lengths smaller than a threshold length, from which a tensile strength estimate can be deduced. The arithmetic mean strength of wood cellulose nanofibrils, which are herein considered representative for all plant fibers, and which exhibit diameters of 3 nm (as measured from X-ray diffraction), amount to 2.3 GPa [20]. Notably, the tensile strength of crystalline  $1\beta$  cellulose, the dominant polymorph for higher-plant cell wall cellulose [14], is even two to three times higher than the reported nanofibril strength, as revealed by means of molecular dynamics [60] of defect-free cellulose. Cellulose nanofibrils with lengths of several hundred nanometers, as the ones tested by Saito et al. [20], however, exhibit defects and/or may contain thin amorphous regions [14], such that the intrinsic strength of crystalline  $1\beta$  cellulose is not reached. In our model, we assume that the nanofibril strength amounts to  $\sigma_{\text{NF,II}}^{\text{ult}} = 2.3$  GPa, as this value already accounts for interfaces/defects present in nanofibrils. The defects, which represent localized weaknesses/breaking points, are not expected to alter density or stiffness of the nanofibrils significantly. Therefore, the properties of crystalline cellulose, given in Table 1 and Eq. (2), are still valid for the nanofibrils.

In this paper we test whether the experimentally determined cellulose nanofibril strength can be upscaled to elastic limits of technical fibers from several different plants. Single fiber tensile tests [13, 61] indicate that stress-strain relations are virtually linear followed by brittle rupture. Marrot et al. [62] observed some minor pre-peak nonlinearities at low stress levels, see Fig. 3, which



can be explained by the progressive alignment of the microfibrils with the fiber axis [63].

Moreover, elasto-brittle failure is also observed in molecular simulations of crystalline cellulose [60].

Given the quasi-brittle failure of cellulose-based fibers and the limited experimental insight, we aim at an engineering approach and consider that the fiber's elastic limit is equal to the fiber strength and that it follows from brittle failure of cellulose nanofibrils. We note that similar elasto-brittle approaches have been very successfully applied to predict the elastic limits and strengths of various composite materials, including cement paste [64], concrete [65], wood [28], plant culms [31] bone [66], or shale [67]. In more detail, we consider that the technical plant fiber remains intact as long as the longitudinal stress of the crystalline cellulose nanofibrils  $\sigma_{\text{NF,II}}$ , obtained from elastic stress concentrations, is smaller than the experimentally determined tensile strength  $\sigma_{\text{NF,II}}^{\text{ult}}$ , which can be mathematically expressed by the failure function  $\mathcal{F}_\sigma$  as

$$\mathcal{F}_\sigma = \sigma_{\text{NF,II}} - \sigma_{\text{NF,II}}^{\text{ult}} \leq 0, \quad (14)$$

Cellulose nanofibril stresses  $\sigma_{\text{NF}}$  are obtained from downscaling the macroscopic uniaxial tensile loading  $\Sigma = \Sigma \underline{e}_L \otimes \underline{e}_L$ , with  $\Sigma > 0$  as macroscopic tensile stress. Therefore, the macrostresses are first translated to macrostrains by applying the inverse form of the generalized Hooke's law  $E = C_{\text{fib}}^{-1} : \Sigma$ , then average

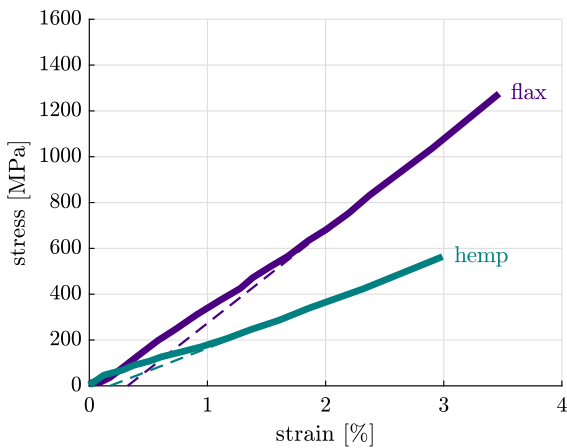


**Fig. 3** Experimental stress-strain relation (continuous lines) obtained from single fiber testing [62]; the dashed lines are a linear extrapolation of the final slope revealing nonlinearities only at small stress levels

phase strains are obtained from step-wise strain downscaling according to the strain concentration relations (4), (6), and (7), and finally cellulose nanofibril phase stresses are obtained by Hooke's law  $\sigma_{\text{NF}} = C_{\text{NF}} : \varepsilon_{\text{NF}}$ , yielding

$$\begin{aligned} \sigma_{\text{NF}}(\varphi) &= C_{\text{NF}} : A_{\text{NF}}^0 : \left( f_{\text{amcel}}^{\text{cel}} \parallel + f_{\text{NF}}^{\text{cel}} A_{\text{NF}}^0 \right)^{-1} : A_{\text{MF}}^0(\varphi) \\ &: \left[ f_{\text{pn}}^{\text{cw}} \parallel + \frac{f_{\text{MF}}^{\text{cw}}}{2\pi} \int_0^{2\pi} C_{\text{MF}} : A_{\text{MF}}^0(\varphi) d\varphi \right]^{-1} \\ &: \left[ f_{\text{cw}}^{\text{cel}} \parallel + f_{\text{lum}}^{\text{cel}} \left( \parallel - P_{\text{cyl}}^{\text{cw}} : C_{\text{cw}} \right)^{-1} \right]^{-1} : C_{\text{fib}}^{-1} \\ &: \Sigma \underline{e}_L \otimes \underline{e}_L. \end{aligned} \quad (15)$$

Notably, the longitudinal nanofibril stress component  $\sigma_{\text{NF,II}}$ , which governs tensile failure according to failure function (14), is constant with respect to the nanofibril's azimuth orientation  $\varphi$ . The sought axial fiber tensile elastic limit  $\Sigma_{\text{fib}}^{\text{ult}}$  corresponds to the macrostress magnitude  $\Sigma$  for which failure criterion (14), evaluated for nanofibril stresses  $\sigma_{\text{NF}}$  according to Eq. (15), becomes zero.

#### 2.4 Plant-specific standard fiber properties and phase volume fractions

Plant-specific physicochemical fiber properties are reported herein, and corresponding phase volume fractions are derived. We focus on 26 of the most common plant fibers reported in the literature, grouped into five fiber types: bast (banana, fiber flax, hemp, isora, jute, kenaf, ramie, sorghum), grass (alfa, bagasse, bamboo), leaf (abaca, curaua, henequen, phormium/harekeke, pineapple, sisal), fruits or seeds (coir, kapok, oil palm), and straw (barley, cornhusk, cornstalk, rice, soybean, wheat). Physicochemical fiber properties depend on the plant species, geographical location, growing conditions, the maturity at harvesting, the exact fiber location within the plant, the fiber extraction process, potential alkali treatment, storage conditions, and several factors related to the testing procedure [5, 9, 68]. To capture this variety, we collect physicochemical properties from several different sources, and report on intervals. In more detail,

minima, representative averages, and maxima for all properties are reported, see Tables 2 and 3, as discussed next.

Average cell wall-related phase volume fractions are derived first, for which physicochemical composition and cellulose crystallinity are discussed next. The cell wall composition of plant fibers has been studied extensively by means of several physicochemical analysis methods, such as acid hydrolysis, chromatography, Klason lignin analysis, and thermogravimetric analysis [112]. This way, (minimum, representative average, and maximum) cell wall-related mass fractions  $\tilde{m}_i^{\text{CW}}$  of (total = crystalline + amorphous) cellulose, hemicellulose, lignin, pectin, ash, and nanoporosity (wax/fat) were measured and

typical results are collected in Table 2. Notably, the reported differences between the representative average and the minimum and maximum values are typically smaller than a few percent. If the sum of average mass fractions exceeds 100 %, phase mass fractions are reduced proportionally through

$$m_i^{\text{CW}} = \frac{\tilde{m}_i^{\text{CW}}}{\sum_j \tilde{m}_j^{\text{CW}}} \quad (16)$$

$$i \in \{\text{totcel, hemcel, lig, pec, ash, npor}\}.$$

If the sum of the average mass fractions is below 100 %, we consider unassigned matter, together with the measured wax/fat mass, as extractive and thus part of the nanoporosity:

**Table 2** Microscopic physicochemical composition in terms of cell wall-related mass fractions  $\tilde{m}_i^{\text{CW}}$  in percent (fractions are not normalized): minimum/**representative average**/maximum values are reported as collected from published experimental data

Name	Type	Total cell.	Hemicell.	Lignin	Pectin	Ash	Nanopore	References
Banana	B	60/71/82	6/10/14	5/8/10	0/4/4	0/5/5	0/0/0	[9, 69, 70]
Flax	B	71/73/81	15/18/21	2/3/3	-1/-	-0/-	-2/-	[9, 68, 71]
Hemp	B	57/70/81	18/20/22	4/5/6	-1/-	-0/-	-1/-	[68, 72, 73]
Isora	B	71/71/75	0/3/3	14/21/23	-0/-	0/0/1	-0/-	[9, 74, 75]
Jute	B	45/58/72	12/18/23	9/18/26	0/0/0	-0/-	-0/-	[9, 68, 72]
Kenaf	B	31/56/81	-22/-	15/17/19	-2/-	-0/-	-0/-	[9, 68, 72]
Ramie	B	69/80/91	5/14/17	1/1/1	-2/-	-0/-	-0/-	[9, 68, 72]
Sorghum	B	-65/-	-19/-	-10/-	-0/-	-5/-	-0/-	[76]
Alfa	G	-45/-	-39/-	-39/-	-0/-	-0/-	-2/-	[9]
Bagasse	G	32/37/48	19/23/28	23/7/32	0/10/10	2/4/5	0/2/4	[9, 69]
Bamboo	G	35/35/47	15/21/23	21/26/31	0/0/0	-0/-	-0/-	[9, 77]
Abaca	L	56/63/70	14/20/25	7/9/12	0/1/1	0/2/2	3/6/6	[9, 68, 78]
Curaua	L	-74/-	-10/-	-8/-	-0/-	-0/-	-1/-	[79]
Henequen	L	60/64/68	18/23/28	8/8/9	-0/-	0/1/1	-5/-	[9, 78]
Phormium	L	-67/-	-30/-	-11/-	-0/-	-0/-	-0/-	[9]
Pineapple	L	70/75/85	-18/-	5/8/12	0/4/4	1/1/1	-0/-	[9, 69, 80]
Sisal	L	38/63/88	10/14/26	8/12/25	0/10/10	-0/-	-3/-	[69, 72, 80, 81]
Coir	F	21/40/46	12/20/31	20/35/47	0/4/4	0/10/10	0/0/9	[9, 69]
Kapok	F	53/59/64	29/30/30	13/17/22	-0/-	1/1/1	-4/-	[82]
Oil Palm	F	43/54/65	17/25/34	13/19/25	0/0/0	1/4/6	-7/-	[11]
Barley	S	31/38/45	27/33/38	14/17/19	-0/-	-0/-	-0/-	[69]
Cornhusk	S	47/54/61	20/32/44	2/3/4	-0/-	3/8/13	-0/-	[83]
Cornstalk	S	38/39/40	-28/-	7/14/21	-0/-	4/0/7	-0/-	[9, 69]
Rice	S	28/32/36	23/26/28	12/13/14	-0/-	14/17/20	-0/-	[69]
Soybean	S	35/85/88	0/5/17	5/11/22	-0/-	1/2/11	-0/-	[84, 85]
Wheat	S	33/36/38	26/29/32	17/18/19	-0/-	2/0/7	-0/-	[69]





**Table 3** Microscopic physicochemical fiber properties related to the minimum/**representative average**/maximum homogenized fiber stiffness/strength: reported microfibril angle,

reported volumetric crystallinity, reported fiber densities, calculated cell wall density according to Eq. (26), and calculated lumen porosity according to Eq. (25)

Name	Type	Microfibril angle		Crystallinity		Density [g/cm <sup>3</sup> ]		lumen	
		$\vartheta$ [°]	References	$\xi_V$ [%]	References	$\rho_{fib}$	References	$\rho_{cw}$	$f_{lpor}^{fib}$ [%]
Banana	B	11/11/12	[86, 87]	30/45/49	[88, 89]	1.3/1.4/1.5	[86]	1.51	14/7/0
Flax	B	5/6/10	[1, 86]	50/78/90	[71, 87, 90, 91]	1.38/1.38/1.5	[86, 92]	1.48	7/7/0
Hemp	B	6/7/10	[1, 86, 93]	50/75/98	[73, 87, 91, 94]	1.35/1.4/1.5	[86, 92, 93]	1.48	9/6/0
Isora	B	20/23/26	[74]	34/71/71	[74, 95]	1.2/1.3/1.3	[12, 96]	1.44	16/9/9
Jute	B	7/8/9	[1, 86, 93]	68/71/73	[89, 97, 98]	1.23/1.35/1.5	[86, 89, 92, 93]	1.42	13/5/0
Kenaf	B	9/12/15	[71, 93]	61/65/69	[71]	1.2/1.22/1.4	[92, 93]	1.45	17/16/3
Ramie	B	6/8/10	[93]	-/64/-	[87]	1.44/1.44/1.55	[86, 92, 93]	1.51	4/4/0
Sorghum	B	16/16/17	[99]	32/43/53	[98–100]	-/0.89/-	[101]	1.5	47/41/35
Alfa	G	-/10/-	*	-/64/-	[102]	-/0.89/-	[12]	1.41	43/37/30
Bagasse	G	14/15/15	[87]	-/48/-	[35]	0.55/1.2/1.25	[86, 92]	1.34	59/10/7
Bamboo	G	2/6/10	[93]	40/56/60	[87, 90]	1.2/1.3/1.5	[103]	1.29	7/0/0
Abaca	L	-/23/-	[87]	-/52/-	[87]	-/1.5/-	[86, 93]	1.45	7/0/0
Curaua	L	15/17/19	[79]	-/66/-	[79]	-/1.4/-	[12]	1.44	12/3/0
Henequen	L	18/20/22	[93]	44/47/50	[104]	1.33/1.4/1.4	[92, 93]	1.45	8/3/3
Phormium	L	-/10/-	*	-/69/-	[105]	-/1.27/-	[106]	1.5	24/15/7
Pineapple	L	6/12/14	[1, 86, 87]	44/52/60	[88]	1.32/1.5/1.56	[12, 86, 92]	1.51	13/1/0
Sisal	L	10/20/25	[1, 86, 87]	68/73/77	[107]	1.2/1.35/1.5	[86, 89, 92, 93]	1.47	19/8/0
Coir	F	30/45/49	[1, 86, 93]	27/30/33	[87]	1.2/1.2/1.25	[2, 86, 89]	1.46	18/18/14
Kapok	F	-/10/-	*	-/46/-	[107]	-/0.38/-	[86]	1.44	76/73/71
Oil Palm	F	-/46/-	[87]	20/25/30	[108]	0.7/1.35/1.55	[87]	1.41	50/4/0
Barley	S	-/10/-	*	-/50/-	*	-/0.52/-	*	1.35	65/61/58
Cornhusk	S	-/10/-	*	48/74/100	[88, 94]	0.43/0.52/0.61	[109]	1.52	72/66/60
Cornstalk	S	-/11/-	[110]	52/76/100	[87, 94]	-/0.52/-	*	1.31	64/60/56
Rice	S	-/10/-	*	40/60/63	[88, 98]	-/1.65/-	[87]	1.43	0/0/0
Soybean	S	-/12/-	[87]	43/47/51	[84, 87]	-/0.52/-	*	1.51	69/66/62
Wheat	S	-/0/-	[111]	48/51/51	[71, 90]	1.45/1.53/1.6	[87]	1.31	0/0/0

\*Assumed

$$m_{npor}^{cw} = 1 - m_{totcel}^{cw} - m_{hemcel}^{cw} - m_{lig}^{cw} - m_{pec}^{cw} - m_{ash}^{cw} \cdot \xi_M = \frac{1}{1 + \left(\frac{1}{\xi_V} - 1\right) \frac{\rho_{amcel}}{\rho_{NF}}}, \quad (18)$$

The cellulose crystallinity is typically given in terms of a volumetric crystallinity index  $\xi_V$  derived from XRD spectra [94]. While accurate values depend on the evaluation method [113], we again report minimum, average, and maximum crystallinity indexes (corresponding to the targeted minimum, average, and maximum prediction) found in the literature, see Table 3. The volumetric crystallinity is related to a crystallinity index by mass,  $\xi_M$ , through

with phase densities  $\rho_{amcel}$  and  $\rho_{NF}$  from Table 1. Cell wall-related mass fraction of crystalline ( $m_{NF}^{cw}$ ) and amorphous ( $m_{amcel}^{cw}$ ) cellulose, respectively, then follow from the total cellulose mass fraction  $m_{totcel}^{cw}$  given in Table 2 and from crystallinity indices  $\xi_M$  according to Eq. (18) as



$$m_{\text{NF}}^{\text{CW}} = \xi_M m_{\text{totcel}}^{\text{CW}}, \quad m_{\text{amcel}}^{\text{CW}} = (1 - \xi_M) m_{\text{totcel}}^{\text{CW}}. \quad f_{\text{pn}}^{\text{CW}} = f_{\text{hemcel}}^{\text{CW}} + f_{\text{lig}}^{\text{CW}} + f_{\text{pec}}^{\text{CW}} + f_{\text{ash}}^{\text{CW}} + f_{\text{npor}}^{\text{CW}}, \quad (19) \quad (21)$$

Corresponding average phase volume fractions for all constituents of the cell walls then read as

$$f_i^{\text{CW}} = \frac{m_i^{\text{CW}} / \rho_i}{\sum_j m_j^{\text{CW}} / \rho_j}, \quad i, j \in \{\text{NF, amcel, hemcel, lig, pec, ash, npor}\}, \quad (20)$$

with phase densities  $\rho_i$  given in Table 1. Average phase volume fractions for the 26 plants are given as bold values in Table 4.

Next, cell wall-related volume fractions associated to both minimum and maximum model predictions, are derived. The maximum fiber stiffness and the maximum fiber strength are obtained for a maximum crystalline cellulose content. This way, we consider that the (normalized) total cellulose mass fraction  $m_{\text{totcel}}^{\text{CW}}$  is equal to the maximum reported mass fractions  $\tilde{m}_{\text{totcel}}^{\text{CW}}$  from Table 2, but at least five percentage points larger than the average cellulose mass fractions. The corresponding mass fractions of all other phases (hemicellulose, lignin, pectin, ash, nanopores) related to the maximum case are obtained by proportionally decreasing the average values. The cellulose crystallinities  $\zeta_V$  for the maximum stiffness/strength case are considered to be equal to the maximum reported cellulose crystallinities from Table 3, but at least five percentage points larger than the average crystallinities. The corresponding phase volume fractions are then calculated through re-evaluation of (18)-(20), see Table 4 for numeric values for all 26 plants. By analogy, the minimum stiffness case relates to minimum reported cellulose mass fractions (but at least five percentage points smaller than their averages) and to minimum reported crystallinities (but at least five percentage points smaller than their averages), see again Table 4 for numeric values.

Volume fractions related to minimum/average/maximum mechanical fiber properties are next assigned to the specific RVEs depicted in Fig. 2. Cell wall-related volume fractions of polymer network ( $f_{\text{pn}}^{\text{CW}}$ ) and of the cellulose microfibrils ( $f_{\text{MF}}^{\text{CW}}$ ) read as

$$f_{\text{MF}}^{\text{CW}} = f_{\text{NF}}^{\text{CW}} + f_{\text{amcel}}^{\text{CW}}. \quad (22)$$

Polymer network-related volume fractions of hemicellulose ( $f_{\text{hemcel}}^{\text{pn}}$ ), lignin ( $f_{\text{lig}}^{\text{pn}}$ ), pectin ( $f_{\text{pec}}^{\text{pn}}$ ), ash ( $f_{\text{ash}}^{\text{pn}}$ ), and nanoporosity ( $f_{\text{npor}}^{\text{pn}}$ ) read as

$$f_i^{\text{pn}} = \frac{f_i^{\text{CW}}}{f_{\text{pn}}^{\text{CW}}}, \quad i \in \{\text{hemcel, lig, pec, ash, npor}\}, \quad (23)$$

and cellulose-related volume fractions of crystalline ( $f_{\text{NF}}^{\text{cel}}$ ) and amorphous ( $f_{\text{amcel}}^{\text{cel}}$ ) cellulose read as

$$f_i^{\text{cel}} = \frac{f_i^{\text{CW}}}{f_{\text{MF}}^{\text{CW}}}, \quad i \in \{\text{NF, amcel}\}. \quad (24)$$

Next, lumen volume fractions at the fiber scale,  $f_{\text{lum}}^{\text{CW}}$ , are derived. Experimentally determined lumen porosities are reported only for a few plant fibers, see e.g. SEM image-based results [114] or density-based results [107]. As a remedy, we back-calculate the lumen porosities from the fiber densities  $\rho_{\text{fib}}$ , which are widely reported in the literature, see Table 3 for corresponding minima, averages, and maxima. As for plants, for which only one single density value is found, we consider intervals of  $\pm 10\%$  around the reported value, to quantify the maximum and minimum, respectively. Considering that the fiber density is the product of cell wall density  $\rho_{\text{CW}}$  and fiber-related cell wall volume fraction  $f_{\text{CW}}^{\text{fib}}$ ,  $\rho_{\text{fib}} = \rho_{\text{CW}} f_{\text{CW}}^{\text{fib}}$  and that  $f_{\text{lum}}^{\text{fib}} + f_{\text{CW}}^{\text{fib}} = 1$  allows for deriving the fiber-related volume fractions  $f_{\text{lum}}^{\text{fib}}$  and  $f_{\text{CW}}^{\text{fib}}$  as

$$f_{\text{CW}}^{\text{fib}} = \frac{\rho_{\text{fib}}}{\rho_{\text{CW}}} \leq 1, \quad f_{\text{lum}}^{\text{fib}} = 1 - \frac{\rho_{\text{fib}}}{\rho_{\text{CW}}} \geq 0, \quad (25)$$

with composition-dependent cell wall density reading as

$$\rho_{\text{CW}} = \sum_i \rho_i f_i^{\text{CW}}, \quad i \in \{\text{NF, amcel, hemcel, lig, pec, ash, npor}\}. \quad (26)$$



**Table 4** Calculated cell wall-related phase volume fractions  $f_i^{CW}$  in percent according to Eq. (20) related to the minimum/**representative average**/maximum homogenized fiber stiffness/strength

Name	Type	Cry. cell.	Am. cell.	Hemicell.	Lignin	Pectin	Ash	Nanopore
Banana	B	18/31/40	41/38/40	14/10/6	13/10/6	5/4/2	5/3/2	5/3/2
Flax	B	32/54/70	32/15/8	21/18/13	4/4/3	1/1/1	0/0/0	10/8/6
Hemp	B	27/50/76	27/17/2	28/20/13	8/6/4	1/1/1	0/0/0	9/7/4
Isora	B	21/46/54	40/19/17	3/3/2	27/24/20	0/0/0	0/0/0	9/8/7
Jute	B	26/37/51	14/16/16	22/18/12	26/20/14	0/0/0	0/0/0	12/9/7
Kenaf	B	17/34/55	11/18/23	33/22/10	29/19/9	3/2/1	0/0/0	7/5/2
Ramie	B	39/49/62	27/28/28	22/14/7	2/1/1	3/2/1	0/0/0	8/5/2
Sorghum	B	19/27/36	40/36/32	22/20/17	13/12/10	0/0/0	4/3/3	2/2/1
Alfa	G	17/21/26	11/12/11	32/30/28	37/35/32	0/0/0	0/0/0	3/3/2
Bagasse	G	12/15/23	16/17/20	23/21/18	8/7/6	9/9/7	3/2/2	30/28/24
Bamboo	G	10/16/24	15/13/16	20/19/16	28/26/22	0/0/0	0/0/0	27/26/22
Abaca	L	24/30/38	27/28/28	23/20/16	12/10/8	1/1/1	2/1/1	11/10/8
Curaua	L	38/45/53	24/23/21	12/10/8	11/9/7	0/0/0	0/0/0	15/13/11
Henequen	L	23/28/34	32/32/31	26/23/20	10/9/8	0/0/0	1/1/1	9/8/7
Phormium	L	34/41/47	20/19/17	32/29/25	14/12/11	0/0/0	0/0/0	0/0/0
Pineapple	L	28/36/50	36/33/34	20/18/9	10/9/5	4/4/2	1/1/0	0/0/0
Sisal	L	23/42/67	11/16/19	22/14/5	21/14/4	15/9/3	0/0/0	8/5/2
Coir	F	5/11/15	15/25/29	23/18/16	46/37/32	4/3/3	7/6/5	0/0/0
Kapok	F	18/23/31	26/27/30	29/27/21	19/17/14	0/0/0	1/1/0	6/6/4
Oil Palm	F	8/11/18	32/34/43	25/22/16	22/19/14	0/0/0	3/2/2	11/10/7
Barley	S	12/17/22	15/17/18	34/31/28	20/18/16	0/0/0	0/0/0	20/18/16
Cornhusk	S	22/39/59	24/14/0	38/33/29	4/4/3	0/0/0	6/6/5	6/5/4
Cornstalk	S	15/25/37	14/8/0	27/25/24	15/15/14	0/0/0	0/0/0	29/28/26
Rice	S	10/18/22	15/12/12	27/26/24	16/15/14	0/0/0	12/11/10	20/19/18
Soybean	S	14/38/45	19/43/42	18/5/3	45/13/9	0/0/0	5/1/1	0/0/0
Wheat	S	12/16/20	14/15/15	28/26/24	20/19/17	0/0/0	0/0/0	26/25/23

Eq. (26) is specialized for average phase volume fractions only, such that the resulting cell wall density is an average quantity, see Table 3. Minimum, average, and maximum fiber-related volume fractions, respectively, then follow from evaluating Eq. (25) with average cell wall densities  $\rho_{CW}$ , but with reported minimum, average, and maximum densities, respectively, see Table 3 for corresponding lumen porosities for all 26 plants. Note that the smallest lumen porosity is related to the maximum stiffness/strength, and vice versa.

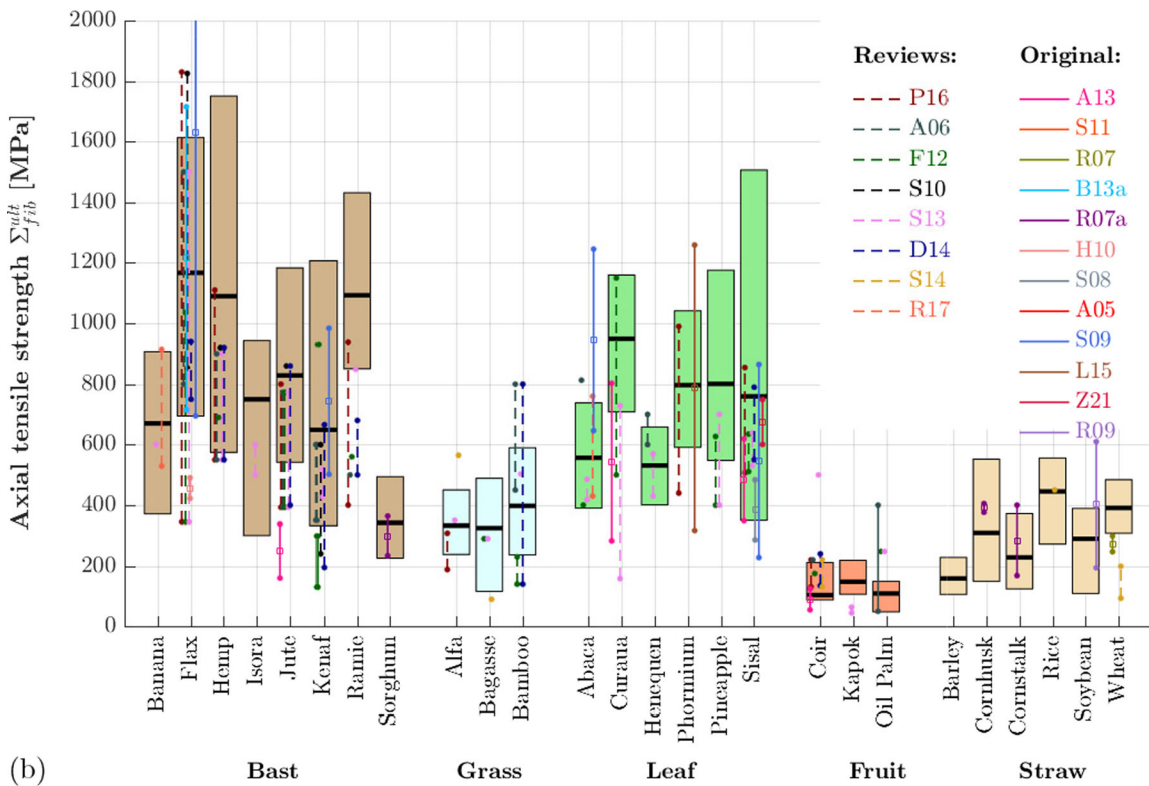
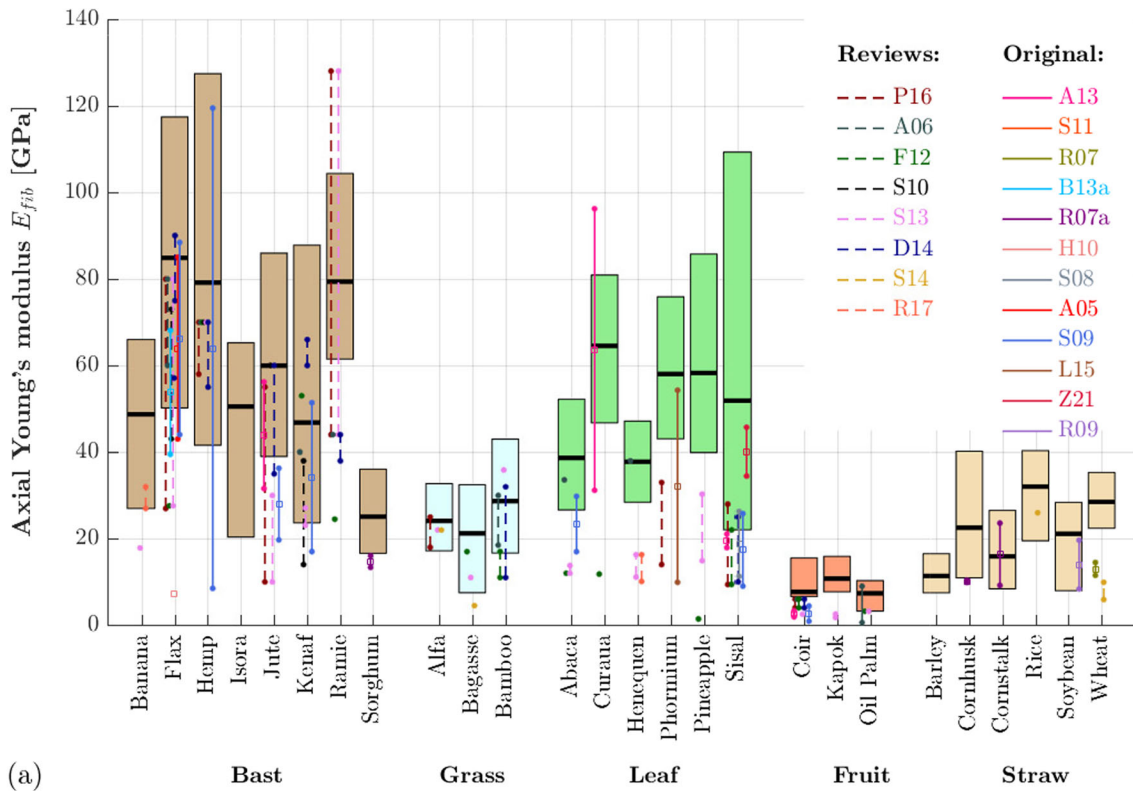
Finally, we report on microfibril angles of the 26 plants introduced in the RVEs of Fig. 2. They range from zero to  $49^\circ$ , see Table 3. If minimum and maximum values are not reported in the database, we

assume a range of  $\pm 3^\circ$  from the reported value. Notably, maximum (or minimum) microfibril angles, yield minimum (or maximum) macroscopic fiber moduli  $E_{fib}$  as well as minimum (or maximum) macroscopic fiber strength  $\Sigma_{fib}^{ult}$ .

### 3 Comparison of model-predicted and experimentally measured fiber stiffness/strength intervals

In order to validate the model-predicted mechanical fiber properties, we first report on published experimental results, obtained from single fiber testing.





◀ **Fig. 4** Model validation for **a** axial Young’s modulus and **b** axial tensile strength: comparison of model predictions (colored bars represent predicted intervals between the minima and maxima modulus/elastic limit, black horizontal lines represent representative averages, see Tables 2–4 for the corresponding minimum/average/maximum physicochemical fiber properties) with experimental data gathered from published reviews (P16...[5], A06...[93], F12...[2], S10...[120], S13...[12], D14...[4], S14...[98], R17...[9]; dashed lines) and from original tests (A13...[10], S11...[11], R07...[71], B13a...[117], R07a...[99], H10...[61], S08...[118], A05...[116], S09...[13], L15...[106], Z21...[119]; continuous lines)

Single fiber testing is a challenge as such, experimental difficulties arise (i) from fiber slippage or imperfect

fiber alignment, see e.g. [13, 115] for more discussion, (ii) from simplification regarding the quantification of the cross section area of the fibers [10, 61], or (iii) from size effects related to gauge lengths [116], which may be removed when accounting for the machine compliance [10]. Given the experimental challenges, reported mechanical properties vary significantly, even more so than the physicochemical properties discussed in Sec. 2.4. In order to cope with this variety, we herein concatenate experimental data from several sources, including original test data [10, 11, 13, 61, 71, 85, 99, 106, 116–119] and data previously collected in review papers [2, 4, 5, 9, 12, 93, 98, 120]. Mechanical properties

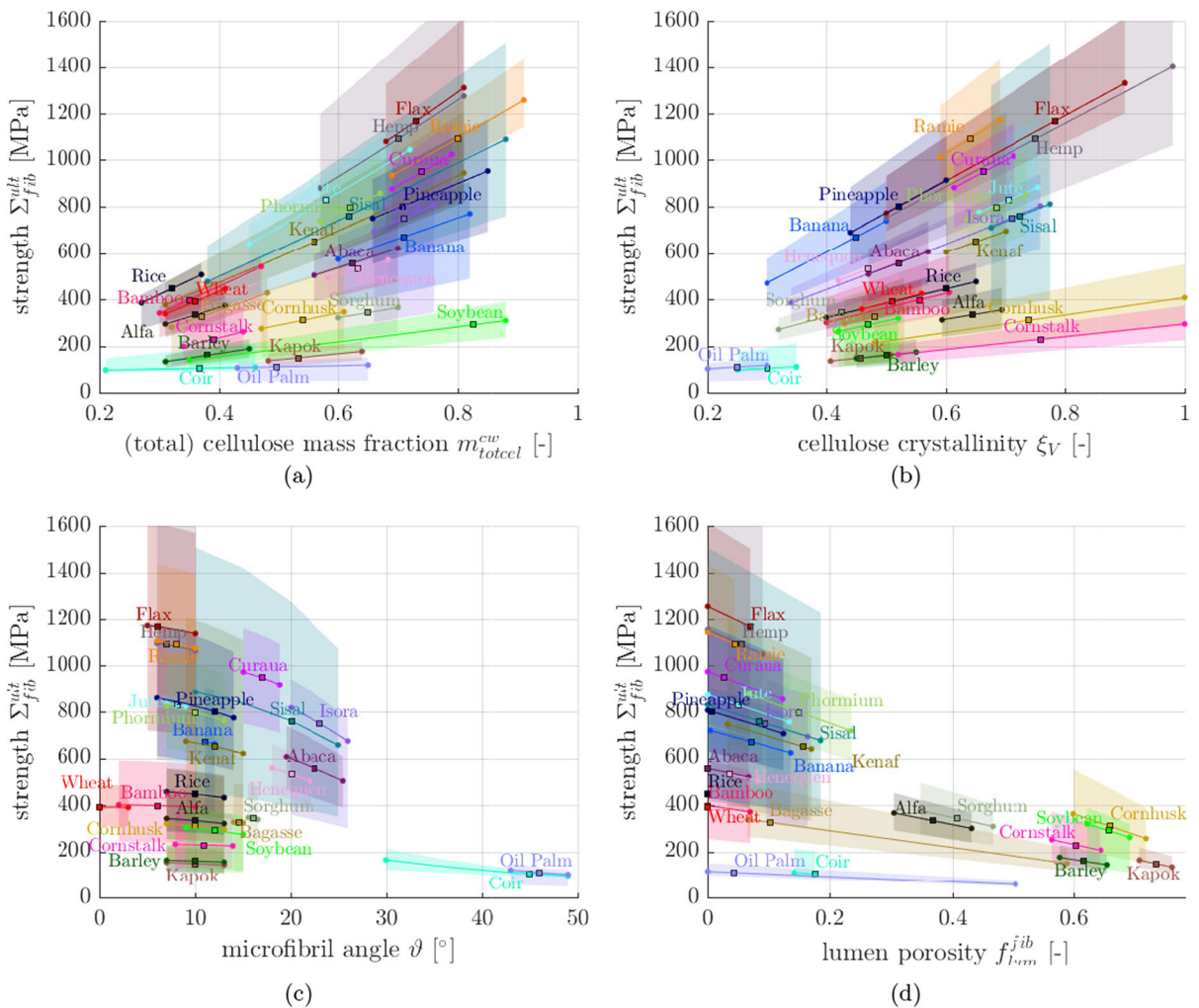


**Fig. 5** Sensitivity of model-predicted fiber strengths with respect to changes of **a** cellulose mass fraction, **b** cellulose crystallinity, **c** microfibril angle, **d** lumen porosity; colored solid

lines refer to average physicochemical properties, colored areas span the intervals between minimum and maximum properties, and square points represent the prediction for average properties



for 25 out of the 26 fibers have been found, data for barley straw fibers is not available. The reported ranges of mechanical properties are depicted in Fig. 4, whereby solid lines refer to original data and dashed lines to data from reviews.

Model-predicted Young's moduli  $E_{\text{fib}}$  and tensile elastic limits  $\Sigma_{\text{fib}}^{\text{ult}}$ , respectively, are obtained from stiffness homogenization according to Eqs. (8–13) and strength homogenization according to Eqs. (14–15), evaluated for plant-specific physicochemical properties given in Tables 2, 3 and 4, and for intrinsic (plant-independent) mechanical phase properties (stiffness according to Table 1, cellulose nanofibril strength according to Sec. 2.3). In Fig. 4, the predicted properties are depicted by colored bars, representing predicted intervals between the minimum and maximum, with black horizontal lines, representing the predicted property from average physicochemical input properties, see Tables 2, 3 and 4 for the corresponding minimum/average/maximum physicochemical fiber properties. Model-predicted ranges for both the elastic modulus and the elastic limit are generally very close to the experimentally measured ranges for elastic modulus and tensile strength, respectively. In more detail, the model is able to reproduce the extraordinarily high mechanical properties seen in most bast fibers, as well as the rather low properties of grass, fruit, and straw fibers. This does corroborate that intrinsic mechanical phase properties gathered from molecular simulations and nanoscale testing can be successfully translated to macroscopic fiber properties—if microstructural features of plant fibers are suitably represented, as done so by the developed multiscale model shown in Fig. 2.

Not all experimentally measured fiber properties fall within the predicted ranges. While predicted and measured strength ranges are generally very close, predicted moduli are typically slightly larger than the experimentally measured ones. This might be explained, on the one hand, by the aforementioned difficulties related to single fiber testing such as fiber slippage, which are likely to affect the stiffness test results more than the strength results, and moreover, always lead to experimental values below the actual elastic fiber modulus [13]. The stiffness overestimation might, on the other hand, be caused by assigning the molecular dynamics-derived stiffness of perfectly regular crystalline cellulose to the nanofibril phase, despite

the interfaces/defects present in nanofibrils [14]. Moreover, some bio-physicochemical features such as sugar contents are not considered in the model, but might partly explain e.g. the smaller experimentally determined moduli and strengths for hemp compared to flax [62, 121]. Modeling the cell wall layers explicitly rather than considering a homogeneous phase, as e.g. done in [24] might also lead to a better performance, but is limited by quantitative experimental data on layer-specific physicochemical properties.

By providing a quantitative link between microstructural features and macroscopic fiber properties, the model further allows us to understand and explore the origin of the observed stiffness and strength differences between the different fibers, as discussed next. Most bast fibers, particularly flax, hemp, and ramie exhibit an outstanding mechanical performance, with predicted average moduli amounting to approximately 90 GPa and predicted average strengths amounting to approximately 1100 MPa. Their microstructure, characterized by high cellulose contents [see Table 2 and the sensitivity diagram in Fig. 5a], high cellulose crystallinities [Table 3 and Fig. 5b], small microfibril angles [Table 3 and Fig. 5c], and small lumen porosities resulting in high fiber densities [Table 3 and Fig. 5d], is tailored to maximize their mechanical performance in fiber direction. The low modulus and strength of sorghum bast fibers, in turn, result mainly from the high lumen porosity. Grass, fruit, and straw fibers exhibit rather low mechanical properties, see Fig. 4. The predicted properties of coir and oil palm fibers are the lowest among the 26 studied fibers, with (average) moduli below 8 GPa and (average) strengths close to 100 MPa, which nicely matches the available experimental data. They both suffer from the highest microfibril angles found in all plant fibers, with averages amounting to roughly 40–45° [see Fig. 5c], coupled with small crystalline cellulose volume fractions [Table 4 and Figs. 5a,b]. Kapok fibers, as well as straw fibers from barley, corn, and soybean exhibit lumen porosities above 60 % (Table 3), which prevents the good mechanical performance of their cell walls to translate to the fiber scale.

Finally, the sensitivity of the fiber strength<sup>1</sup> with respect to changes of the fibers' physicochemical properties is discussed. The dependencies are studied

<sup>1</sup> The sensitivity of the fiber stiffness is very similar to the one of the strength and is therefore not discussed in detail



for four significant input properties: (a) the cell wall-related mass fraction of (crystalline + amorphous = total) cellulose  $m_{\text{totcel}}^{\text{cw}}$ , (b) the volumetric cellulose crystallinity  $\xi_V$ , (c) the microfibril angle  $\vartheta$ , and (d) the lumen porosity  $f_{\text{lum}}^{\text{fib}}$ . In more detail, we consider that one of the four properties exhibits values bound by the interval between minimum and maximum values reported in the literature (see Tables 2 and 3). Considering that all other physicochemical properties exhibit average input values, we arrive at the solid lines in the fiber-specific influence diagrams shown in Fig. 5. Considering, in turn, that all other input properties still maintain their variability within the corresponding intervals, we obtain the fiber-specific colored areas of Fig. 5. The strengths of all 26 fibers monotonously increase with increasing cellulose mass fractions, with increasing crystallinity, with decreasing microfibril angle, and with decreasing lumen porosity. Moreover, Fig. 5 reveals the origin of the variability of the predicted strength results. A significant share of the variability results from the broad intervals of the cellulose mass fractions, which originate e.g. from different fiber extraction methods. This shows that increasing the cellulose content of fibers, e.g. by means of chemical treatments to remove wax, hemicellulose, and/or lignin, is a very effective way of enhancing the fiber strength, as corroborated by single fiber tests [122, 123]. The microfibril angle, in turn, even though its actual quantity has a significant importance, typically ranges within narrow intervals (except for Sisal), such that the variability of the microfibril angle has little effect on the strength variability.

#### 4 Conclusions and outlook

An established multiscale modeling framework for natural fibers based on continuum micromechanics [25, 27, 30] is herein adopted to predict the axial mechanical properties of 26 of the most commonly used plant fibers. Relying on a plant-independent microstructural representation but plant-specific physicochemical fiber properties, which even for a given plant species may vary considerably, nanoscale mechanical cellulose properties (170 GPa axial modulus, 2300 MPa axial strength) are upscaled to the macroscopic fiber scale. In more detail, we predict

upper and lower bounds of the axial mechanical fiber properties, based on reported intervals of physicochemical input properties. Predicted axial mechanical properties amount to moduli below 10 GPa and strengths below 100 MP for fibers with large microfibril angles, high lumen porosities, and/or low (crystalline) cellulose contents, as found in fibers from fruits, seeds, and straws. However, predicted moduli can be as high as 120 GPa and predicted strengths can be as high as 1600 MP for bast fibers with ideal physicochemical properties regarding stiffness and strength in the longitudinal direction. The predicted bounds, for almost all 26 studied plant fibers, frame the experimentally determined fiber stiffnesses and strengths, respectively, which were gathered from published single fiber test campaigns. This way, we corroborate that both the reduction of the mechanical performance upon transition from the nanoscale to the macroscale as well as the differences in mechanical properties among the fibers from different plants can be assessed quantitatively when incorporating the main microstructural features such as microfibril angle, cellulose crystallinity, and lumen porosity.

Future work aims at expanding this micromechanics model to biocomposites by including yet another macroscopic scale of observation. At this scale, plant fibers of any orientation are interacting with the surrounding matrix phase, whereby modeling of imperfect bonding at fiber-matrix interfaces might be incorporated. In this sense, the proposed model for plant fibers is intended as a contribution to the three-dimensional mechanical description of biocomposites, which may pave the way to new and improved composite formulations. A reliable description of the mechanical composite behavior is particularly important for developing and optimizing lightweight construction elements from such materials. Moreover, emphasis should be also put on incorporating fracture mechanics and stochastics into the description of the failure process of cellulose-based fibers, supported by novel experimental characterization attempts of cellulose nanofibrils.

**Acknowledgements** The authors gratefully acknowledge the financial support by the Austrian Science Fund (FWF) through the SFB F77 project and the START project Y1093-N30.

**Funding** Open access funding provided by Austrian Science Fund (FWF).



**Open Access** This article is licensed under a Creative Commons Attribution 4.0 International License, which permits use, sharing, adaptation, distribution and reproduction in any medium or format, as long as you give appropriate credit to the original author(s) and the source, provide a link to the Creative Commons licence, and indicate if changes were made. The images or other third party material in this article are included in the article's Creative Commons licence, unless indicated otherwise in a credit line to the material. If material is not included in the article's Creative Commons licence and your intended use is not permitted by statutory regulation or exceeds the permitted use, you will need to obtain permission directly from the copyright holder. To view a copy of this licence, visit <http://creativecommons.org/licenses/by/4.0/>.

## Appendix A: hill tensors

We deal with Eshelby problems involving spheroidal inclusions  $i$  in matrices with stiffness tensor  $\mathbb{C}_m$ . Associated Hill tensors  $\mathbb{P}_i^m$ , required for micromechanics homogenization and concentration relations according to Eqs. (8–13), read as

$$\mathbb{P}_i^m = \mathbb{S}_i^m : \mathbb{C}_m^{-1}, \quad (\text{A1})$$

whereby  $\mathbb{S}_i^m$  denotes the Eshelby tensor and is a function of the inclusion's shape (cylindrical  $i = \text{cyl}$ , or spherical  $i = \text{sph}$ ) and of the matrix' Poisson's ratio  $\nu_m$  [52]. As for spherical inclusions embedded in a polymer network matrix, the Eshelby tensor components read as [32]

$$\begin{aligned} S_{\text{sph},ijkl}^{\text{pm}} = & \frac{5\nu_{\text{pm}} - 1}{15(1 - \nu_{\text{pm}})} \delta_{ij} \delta_{kl} + \\ & \frac{4 - 5\nu_{\text{pm}}}{15(1 - \nu_{\text{pm}})} (\delta_{ik} \delta_{jl} + \delta_{il} \delta_{jk}), \end{aligned} \quad (\text{A2})$$

with  $\delta_{ij}$  denoting the Kronecker delta. As for the cylindrical cellulose inclusions (nanofibrils and microfibrils, respectively), the infinite matrix in the corresponding Eshelby problem is isotropic, such that non-zero components with respect to the local orthonormal coordinate base  $x_1, x_2, x_3$  (with  $x_3$  as the cylinder axis direction) read as [124]

$$\begin{aligned} S_{\text{cyl},2222}^m = S_{\text{cyl},3333}^m &= \frac{5 - 4\nu_m}{8(1 - \nu_m)} \\ S_{\text{cyl},2233}^m = S_{\text{cyl},3322}^m &= \frac{-1 + 4\nu_m}{8(1 - \nu_m)} \\ S_{\text{cyl},1313}^m = S_{\text{cyl},1212}^m &= \frac{1}{4} \\ S_{\text{cyl},2323}^m &= \frac{3 - 4\nu_m}{8(1 - \nu_m)}, \end{aligned} \quad (\text{A3})$$

whereby  $m$  stands either for the amorphous cellulose matrix (for nanofibril inclusions), or for the polymer network matrix (for microfibril inclusions). As for the cylindrical lumen pores, the infinite matrix in the corresponding Eshelby problem is transversally isotropic, whereby the cylinder axis is aligned with the matrix' axis of transverse symmetry. This way, the the Eshelby tensor reads as [125]

$$\begin{aligned} \mathbb{S}_{\text{cyl}}^{\text{cw}} = & \frac{C_{\text{cw},1}}{2C_{\text{cw},1} + C_{\text{cw},2}} \mathbb{T}^{(1)} + \frac{C_{\text{cw},1} + C_{\text{cw},2}}{2C_{\text{cw},1} + C_{\text{cw},2}} \mathbb{T}^{(2)} \\ & + \frac{C_{\text{cw},3}}{2C_{\text{cw},1} + C_{\text{cw},2}} \mathbb{T}^{(3)} + \mathbb{T}^{(5)}. \end{aligned} \quad (\text{A4})$$

With  $x_3$  as the axis of transverse symmetry, tensors  $T^{(1)}, \dots, T^{(5)}$  have the following non-zero components

$$\begin{aligned} T_{1111}^{(1)} = T_{2222}^{(1)} = T_{1122}^{(1)} = T_{2211}^{(1)} &= 1 \\ T_{1212}^{(2)} = T_{2121}^{(2)} = T_{1221}^{(2)} = T_{2112}^{(2)} = T_{1111}^{(2)} = T_{2222}^{(2)} &= \\ -T_{1122}^{(2)} = -T_{2211}^{(2)} &= \frac{1}{2} \\ T_{1133}^{(3)} = T_{2233}^{(3)} &= 1 \\ T_{1313}^{(5)} = T_{2323}^{(5)} = T_{1331}^{(5)} = T_{2332}^{(5)} = T_{3113}^{(5)} = T_{3223}^{(5)} &= \\ T_{3131}^{(5)} = T_{3132}^{(5)} &= \frac{1}{4}. \end{aligned} \quad (\text{A5})$$

and  $C_{\text{cw},1}$ ,  $C_{\text{cw},2}$ , and  $C_{\text{cw},3}$  read as

$$\begin{aligned} C_{\text{cw},1} &= (C_{\text{cw},1111} + C_{\text{cw},1122})/2, \\ C_{\text{cw},2} &= 2C_{\text{cw},1212}, \\ C_{\text{cw},3} &= C_{\text{cw},1133}, \end{aligned} \quad (\text{A6})$$





## References

- Bledzki AK, Gassan J (1999) Composites reinforced with cellulose based fibres. *Prog Polym Sci* 24(2):221–274. [https://doi.org/10.1016/S0079-6700\(98\)00018-5](https://doi.org/10.1016/S0079-6700(98)00018-5)
- Faruk O, Bledzki AK, Fink H-P, Sain M (2012) Biocomposites reinforced with natural fibers: 2000–2010. *Prog Polym Sci* 37(11):1552–1596. <https://doi.org/10.1016/j.progpolymsci.2012.04.003>
- Oksman K, Skrifvars M, Selin JF (2003) Natural fibres as reinforcement in polylactic acid (PLA) composites. *Compos Sci Technol* 63(9):1317–1324. [https://doi.org/10.1016/S0266-3538\(03\)00103-9](https://doi.org/10.1016/S0266-3538(03)00103-9)
- Dicker MP et al (2014) Green composites: a review of material attributes and complementary applications. *Compos Part A Appl Sci Manuf* 56:280–289. <https://doi.org/10.1016/j.compositesa.2013.10.014>
- Pickering KL, Efendy MG, Le TM (2016) A review of recent developments in natural fibre composites and their mechanical performance. *Compos Part A Appl Sci Manuf* 83:98–112
- tak Lau K, yan Hung P, Zhu MH, Hui D, (2018) Properties of natural fibre composites for structural engineering applications. *Compos Part B Eng* 136:222–233. <https://doi.org/10.1016/j.compositesb.2017.10.038>
- Mohanty AK, Misra M, Hinrichsen G (2000) Biofibres, biodegradable polymers and biocomposites: an overview. *Macromol Mater Eng* 276–277:1–24
- Bengtsson M, Baillif ML, Oksman K (2007) Extrusion and mechanical properties of highly filled cellulose fibre-polypropylene composites. *Compos Part A Appl Sci Manuf* 38(8):1922–1931. <https://doi.org/10.1016/j.compositesa.2007.03.004>
- Ramesh M, Palanikumar K, Reddy KH (2017) Plant fibre based bio-composites: sustainable and renewable green materials. *Renew Sustain Energy Rev* 79(February):558–584. <https://doi.org/10.1016/j.rser.2017.05.094>
- Alves Fidelis ME, Pereira TVC, Gomes ODFM, De Andrade Silva F, Toledo Filho RD (2013) The effect of fiber morphology on the tensile strength of natural fibers. *J Mater Res Technol* 2(2):149–157. <https://doi.org/10.1016/j.jmrt.2013.02.003>
- Shinoy S, Visvanathan R, Panigrahi S, Kochubabu M (2011) Oil palm fiber (OPF) and its composites: a review. *Ind Crops Prod* 33(1):7–22. <https://doi.org/10.1016/j.indcrop.2010.09.009>
- Sathishkumar TP, Navaneethakrishnan P, Shankar S, Rajasekar R, Rajini N (2013) Characterization of natural fiber and composites—a review. *J Reinf Plast Compos* 32(19):1457–1476. <https://doi.org/10.1177/0731684413495322>
- Symington MC, Banks WM, West OD, Pethrick RA (2009) Tensile testing of cellulose based natural fibers for structural composite applications MAR. *J Compos Mater*. <https://doi.org/10.1177/0021998308097740>
- Moon RJ, Martini A, Nairn J, Simonsen J, Youngblood J (2011) Cellulose nanomaterials review: structure, properties and nanocomposites. *Chem Soc Rev* 40(7):3941–3994. <https://doi.org/10.1039/c0cs00108b>
- Osorio L et al (2018) In-depth study of the microstructure of bamboo fibres and their relation to the mechanical properties. *J Reinf Plast Compos* 37(17):1099–1113. <https://doi.org/10.1177/0731684418783055>
- Manthey NW, Cardona F, Francucci G, Aravinthan T (2013) Thermo-mechanical properties of epoxidized hemp oil-based bioresins and biocomposites. *J Reinf Plast Compos* 32(19):1444–1456. <https://doi.org/10.1177/0731684413493030>
- Ansell M, Mwaikambo L (2009) In: *The structure of cotton and other plant fibres*, vol 2. Elsevier, pp 62–94
- Tashiro K, Kobayashi M (1985) Calculation of crystallite modulus of native cellulose. *Polym Bull* 14(3–4):213–218. <https://doi.org/10.1007/BF00254940>
- Dri FL et al (2014) Anisotropy and temperature dependence of structural, thermodynamic, and elastic properties of crystalline cellulose I $\beta$ : a first-principles investigation. *Model Simul Mater Sci Eng*. <https://doi.org/10.1088/0965-0393/22/8/085012>
- Saito T, Kuramae R, Wohlert J, Berglund LA, Isogai A (2013) An ultrastrong nanofibrillar biomaterial: the strength of single cellulose nanofibrils revealed via sonication-induced fragmentation. *Biomacromol* 14(1):248–253. <https://doi.org/10.1021/bm301674e>
- Hearle JW (1963) The fine structure of fibers and crystalline polymers. I. Fringed fibril structure. *J Appl Polym Sci* 7(4):1175–1192. <https://doi.org/10.1002/app.1963.070070401>
- Salmen L, De Ruvo A (1985) A model for the prediction of fiber elasticity. *Wood Fiber Sci* 17(3):336–350
- Gassan J, Chate A, Bledzki AK (2001) Calculation of elastic properties of natural fibers. *J Mater Sci* 36(15):3715–3720. <https://doi.org/10.1023/A:1017969615925>
- Sun Z, Zhao X, Wang X, Ma J (2014) Multiscale modeling of the elastic properties of natural fibers based on a generalized method of cells and laminate analogy approach. *Cellulose* 21(3):1135–1141. <https://doi.org/10.1007/s10570-014-0201-y>
- Hofstetter K, Hellmich C, Eberhardsteiner J (2005) Development and experimental validation of a continuum micromechanics model for the elasticity of wood. *Eur J Mech A Solids* 24(6):1030–1053. <https://doi.org/10.1016/j.euromechsol.2005.05.006>
- Hofstetter K, Hellmich C, Eberhardsteiner J (2006) The influence of the microfibril angle on wood stiffness: a continuum micromechanics approach. *Comput Assist Mech Eng Sci* 13(4):523–536
- Bader TK, Hofstetter K, Hellmich C, Eberhardsteiner J (2011) The poroelastic role of water in cell walls of the hierarchical composite “softwood”. *Acta Mech* 217(1–2):75–100
- Hofstetter K, Hellmich C, Eberhardsteiner J, Mang HA (2008) Micromechanical estimates for elastic limit states in wood materials, revealing nanostructural failure mechanisms. *Mech Adv Mater Struct* 15(6–7):474–484. <https://doi.org/10.1080/15376490802142387>
- Bader TK, Hofstetter K, Hellmich C, Eberhardsteiner J (2010) Poromechanical scale transitions of failure stresses in wood: from the lignin to the spruce level. *ZAMM Zeitschrift für Angew Math und Mech*



- 90(10–11):750–767. <https://doi.org/10.1002/zamm.201000045>
30. Gangwar T, Schillinger D (2019) Microimaging-informed continuum micromechanics accurately predicts macroscopic stiffness and strength properties of hierarchical plant culm materials. *Mech Mater* 130(January):39–57. <https://doi.org/10.1016/j.mechmat.2019.01.009>
  31. Gangwar T et al (2021) Multiscale characterization and micromechanical modeling of crop stem materials. *Bio-mech Model Mechanobiol* 20(1):69–91. <https://doi.org/10.1007/s10237-020-01369-6>
  32. Zaoui A (2002) Continuum micromechanics: survey. *J Eng Mech* 128(8):808–816
  33. Hofstetter K, Hellmich C, Eberhardsteiner J (2006) Continuum micromechanics estimation of wood strength. *PAMM* 6(1):75–78. <https://doi.org/10.1002/pamm.200610020>
  34. Donaldson L (2008) Microfibril angle: measurement, variation and relationships—a review. *IAWA J* 29(4):345–386. <https://doi.org/10.1163/22941932-90000192>
  35. Štiligoj M, Hribernik S, Stana K, Kree T (2013) Plant fibres for textile and technical applications. *Adv Agrophys Res*. <https://doi.org/10.5772/52372>
  36. Sakurada I, Kaji K (1969) Experimental determination of elastic moduli of the crystalline regions in oriented polymers. *Kobunshi Kagaku* 26(296):817–822. <https://doi.org/10.1295/koron1944.26.817>
  37. Nishino T, Takano K, Nakamae K (1995) Elastic modulus of the crystalline regions of cellulose polymorphs. *J Polym Sci Part B Polym Phys* 33(11):1647–1651. <https://doi.org/10.1002/polb.1995.090331110>
  38. Diddens I, Murphy B, Krisch M, Müller M (2008) Anisotropic elastic properties of cellulose measured using inelastic X-ray scattering. *Macromolecules* 41(24):9755–9759. <https://doi.org/10.1021/ma801796u>
  39. Iwamoto S, Kai W, Isogai A, Iwata T (2009) Elastic modulus of single cellulose microfibrils from tunicate measured by atomic force microscopy. *Biomacromol* 10(9):2571–2576. <https://doi.org/10.1021/bm900520n>
  40. Šturcová A, Davies GR, Eichhorn SJ (2005) Elastic modulus and stress-transfer properties of tunicate cellulose whiskers. *Biomacromol* 6(2):1055–1061. <https://doi.org/10.1021/bm049291k>
  41. Tanaka F, Iwata T (2006) Estimation of the elastic modulus of cellulose crystal by molecular mechanics simulation. *Cellulose* 13(5):509–517. <https://doi.org/10.1007/s10570-006-9068-x>
  42. Kulasinski K, Keten S, Churakov SV, Derome D, Carmeliet J (2014) A comparative molecular dynamics study of crystalline, paracrystalline and amorphous states of cellulose. *Cellulose* 21(3):1103–1116. <https://doi.org/10.1007/s10570-014-0213-7>
  43. Cowin SC, Mehrabadi MM (1992) The structure of the linear anisotropic elastic symmetries. *J Mech Phys Solids* 40(7):1459–1471
  44. O'Sullivan AC (1997) Cellulose: the structure slowly unravels. *Cellulose* 4(3):173–207. <https://doi.org/10.1023/A:1018431705579>
  45. Chen H (2014) *Biotechnology of lignocellulose*. Springer, Netherlands, Dordrecht, Netherlands
  46. Youssefian S, Jakes JE, Rahbar N (2017) Variation of nanostructures, molecular interactions, and anisotropic elastic moduli of lignocellulosic cell walls with moisture. *Sci Rep* 7(1):2054. <https://doi.org/10.1038/s41598-017-02288-w>
  47. Cousins WJ (1978) Young's modulus of hemicellulose as related to moisture content. *Wood Sci Technol* 12(3):161–167. <https://doi.org/10.1007/BF00372862>
  48. Cousins WJ (1976) Elastic modulus of lignin as related to moisture content. *Wood Sci Technol* 10(1):9–17
  49. Salbu L (2011) Compressibility and compactibility of pectin powders—a study of their potential as direct compression excipients in tablets. Ph.D. thesis, University of Tromsø
  50. Pabst W, Gregorová E (2013) Elastic properties of silica polymorphs—a review. *Ceram Silik* 57(3):167–184
  51. Hill R (1963) Elastic properties of reinforced solids: some theoretical principles. *J Mech Phys solid solids* 11:357–372
  52. Eshelby JD (1957) The determination of the elastic field of an ellipsoidal inclusion, and related problems. *Proc R Soc London Ser A* 241(1226):376–396
  53. Hershey AVADV (1954) The elasticity of an isotropic aggregate of anisotropic cubic crystals. *J Appl Mech* 21(3):236–240. <https://doi.org/10.1002/prca.201200064>
  54. Kröner E (1958) Berechnung der elastischen Konstanten des Vielkristalls aus den Konstanten des Einheitskristalls [Computation of the elastic constants of a polycrystal based on the constants of the single crystal]. *Z. für Phys A Hadron Nucl* 151(4):504–518
  55. Mori T, Tanaka K (1973) Average stress in matrix and average elastic energy of materials with misfitting inclusions. *Acta Metall* 21(5):571–574. [https://doi.org/10.1016/0001-6160\(73\)90064-3](https://doi.org/10.1016/0001-6160(73)90064-3)
  56. Benveniste Y (1987) A new approach to the application of Mori-Tanaka's theory in composite materials. *Mech Mater* 6(2):147–157. [https://doi.org/10.1016/0167-6636\(87\)90005-6](https://doi.org/10.1016/0167-6636(87)90005-6)
  57. Schjødt-Thomsen J, Pyrz R (2001) The Mori-Tanaka stiffness tensor: diagonal symmetry, complex fibre orientations and non-dilute volume fractions. *Mech Mater* 33(10):531–544. [https://doi.org/10.1016/S0167-6636\(01\)00072-2](https://doi.org/10.1016/S0167-6636(01)00072-2)
  58. Sevostianov I, Kachanov M (2014) On some controversial issues in effective field approaches to the problem of the overall elastic properties. *Mech Mater* 69(1):93–105. <https://doi.org/10.1016/j.mechmat.2013.09.010>
  59. Lee HR, Kim KH, Mun SC, Chang YK (2018) A new method to produce cellulose nanofibrils from microalgae and the measurement of their mechanical strength. *Carbohydr Polym* 180(July):276–285. <https://doi.org/10.1016/j.carbpol.2017.09.104>
  60. Wu X, Moon RJ, Martini A (2014) Tensile strength of I $\beta$  crystalline cellulose predicted by molecular dynamics simulation. *Cellulose* 21(4):2233–2245. <https://doi.org/10.1007/s10570-014-0325-0>
  61. Hu W, Ton-That M-T, Perrin-Sarazin F, Denault J (2010) An improved method for single fiber tensile test of natural fibers. *Polym Eng Sci* 50(4):819–825. <https://doi.org/10.1002/pen.21593>



62. Marrot L, Lefevvre A, Pontoire B, Bourmaud A, Baley C (2013) Analysis of the hemp fiber mechanical properties and their scattering. *Ind Crop Prod* 51:317–327. <https://doi.org/10.1016/j.indcrop.2013.09.026>
63. Baley C (2002) Analysis of the flax fibres tensile behaviour and analysis of the tensile stiffness increase. *Compos Part A Appl Sci Manuf* 33(7):939–948. [https://doi.org/10.1016/S1359-835X\(02\)00040-4](https://doi.org/10.1016/S1359-835X(02)00040-4)
64. Pichler B, Hellmich C (2011) Upscaling quasi-brittle strength of cement paste and mortar: a multi-scale engineering mechanics model. *Cem Concr Res* 41(5):467–476. <https://doi.org/10.1016/j.cemconres.2011.01.010>
65. Königsberger M et al (2018) Hydrate failure in ITZ governs concrete strength: a micro-to-macro validated engineering mechanics model. *Cem Concr Res* 103:77–94. <https://doi.org/10.1016/j.cemconres.2017.10.002>
66. Fritsch A, Hellmich C, Dormieux L (2009) Ductile sliding between mineral crystals followed by rupture of collagen crosslinks: experimentally supported micromechanical explanation of bone strength. *J Theor Biol* 260(2):230–252. <https://doi.org/10.1016/j.jtbi.2009.05.021>
67. Bobko CP et al (2011) The nanogranular origin of friction and cohesion in shale—a strength homogenization approach to interpretation of nanoindentation results. *Int J Numer Anal Methods Geomech* 35(17):1854–1876. <https://doi.org/10.1002/nag.984>
68. Ramamoorthy SK, Skrifvars M, Persson A (2015) A review of natural fibers used in biocomposites: plant, animal and regenerated cellulose fibers. *Polym Rev* 55(1):107–162. <https://doi.org/10.1080/15583724.2014.971124>
69. Onuaguluchi O, Banthia N (2016) Plant-based natural fibre reinforced cement composites: a review. *Cem Concr Compos* 68:96–108. <https://doi.org/10.1016/j.cemconcomp.2016.02.014>
70. Cherian BM et al (2008) A novel method for the synthesis of cellulose nanofibril whiskers from banana fibers and characterization. *J Agric Food Chem* 56(14):5617–5627. <https://doi.org/10.1021/jf8003674>
71. Reddy N, Yang Y (2007) Preparation and characterization of long natural cellulose fibers from wheat straw. *J Agric Food Chem* 55(21):8570–8575. <https://doi.org/10.1021/jf071470g>
72. Li X, Tabil LG, Panigrahi S (2007) Chemical treatments of natural fiber for use in natural fiber-reinforced composites: a review. *J Polym Environ* 15(1):25–33. <https://doi.org/10.1007/s10924-006-0042-3>
73. Wang B, Sain M, Oksman K (2007) Study of structural morphology of hemp fiber from the micro to the nanoscale. *Appl Compos Mater* 14(2):89–103. <https://doi.org/10.1007/s10443-006-9032-9>
74. Zimniewska M, Wladyka-Przybylak M, Mankowski J (2011) In: Kalia S, Kaith B, Kaur I (eds) Cellulose fibers: bio- and nano-polymer composites Cellul. Fibers Bio-Nano-Polymer Compos. Springer, p 97–119
75. Chirayil CJ et al (2014) Isolation and characterization of cellulose nanofibrils from *Helicteres isora* plant. *Ind Crops Prod* 59:27–34. <https://doi.org/10.1016/j.indcrop.2014.04.020>
76. Saeed HA, Liu Y, Lucia LA, Chen H (2017) Evaluation of Sudanese sorghum and bagasse as a pulp and paper feedstock. *BioResources* 12(3):5212–5222. <https://doi.org/10.15376/biores.12.3.5212-5222>
77. Azeez MA, Orege JI (2018) In: Abdul Khalil H (ed) Bamboo, its chemical modification and products. *Bamboo Curr. Futur. Prospect*. IntechOpen, pp 25–48
78. Tarrés Q et al (2019) Interface and micromechanical characterization of tensile strength of bio-based composites from polypropylene and henequen strands. *Ind Crops Prod* 132:319–326. <https://doi.org/10.1016/j.indcrop.2019.02.010>
79. Tomczak F, Satyanarayana KG, Sydenstricker THD (2007) Studies on lignocellulosic fibers of Brazil: part III—morphology and properties of Brazilian curauá fibers. *Compos Part A Appl Sci Manuf* 38(10):2227–2236. <https://doi.org/10.1016/j.compositesa.2007.06.005>
80. Mishra S, Mohanty AK, Drzal LT, Misra M, Hinrichsen G (2004) A review on pineapple leaf fibers, sisal fibers and their biocomposites. *Macromol Mater Eng* 289(11):955–974. <https://doi.org/10.1002/mame.200400132>
81. Joseph P, Joseph K, Thomas S (1999) Effect of processing variables on the mechanical properties of sisal-fiber-reinforced polypropylene composites. *Compos Sci Technol* 59(11):1625–1640. [https://doi.org/10.1016/S0266-3538\(99\)00024-X](https://doi.org/10.1016/S0266-3538(99)00024-X)
82. Draman SFS, Daik R, Latif FA, El-Sheikh SM (2014) Characterization and thermal decomposition kinetics of kapok (*Ceiba pentandra* L.)—based cellulose. *Bioresources* 9(1):8–23. <https://doi.org/10.15376/biores.9.1.8-23>
83. Pandecha K, Pongtornkulpanich A, Sukchai S, Suriwong T (2015) Thermal properties of corn husk fiber as insulation for flat plate solar collector. *J Renew Energy Smart Grid Technol* 10(1):27–36
84. Martelli-Tosi M et al (2017) Chemical treatment and characterization of soybean straw and soybean protein isolate/straw composite films. *Carbohydr Polym* 157:512–520. <https://doi.org/10.1016/j.carbpol.2016.10.013>
85. Reddy N, Yang Y (2009) Natural cellulose fibers from soybean straw. *Bioresour Technol* 100(14):3593–3598. <https://doi.org/10.1016/j.biortech.2008.09.063>
86. Mwaikambo L (2006) Review of the history, properties and application of plant fibres. *Afr J Sci Technol* 7(2):121
87. Djafari Petroudy S (2017) In: Physical and mechanical properties of natural fibers. Elsevier, pp 59–83
88. Reddy N, Yang Y (2005) Biofibers from agricultural byproducts for industrial applications. *Trends Biotechnol* 23(1):22–27. <https://doi.org/10.1016/j.tibtech.2004.11.002>
89. Devireddy SBR, Biswas S (2017) Physical and mechanical behavior of unidirectional banana/jute fiber reinforced epoxy based hybrid composites. *Polym Compos* 38(7):1396–1403. <https://doi.org/10.1002/pc.23706>
90. Chen W et al (2011) Isolation and characterization of cellulose nanofibers from four plant cellulose fibers using a chemical-ultrasonic process. *Cellulose* 18(2):433–442. <https://doi.org/10.1007/s10570-011-9497-z>



91. Madsen B, Gamstedt EK (2013) Wood versus plant fibers: similarities and differences in composite applications. *Adv Mater Sci Eng*. <https://doi.org/10.1155/2013/564346>
92. Rowell RM (2008) Natural fibres: types and properties. *Perform Nat Compos*. <https://doi.org/10.1533/9781845694593.1.3>
93. André A (2006) *Fibres for Strengthening of Timber Structures*. Luleå University of Technology, Department of Civil and Environmental Engineering, Tech. Rep
94. Thygesen A, Oddershede J, Lilholt H, Thomsen AB, Ståhl K (2005) On the determination of crystallinity and cellulose content in plant fibres. *Cellulose* 12(6):563–576. <https://doi.org/10.1007/s10570-005-9001-8>
95. Joy J et al (2016) Preparation and characterization of poly(butylene succinate) bionanocomposites reinforced with cellulose nanofiber extracted from *Helicteres isora* plant. *J Renew Mater* 4(5):351–364. <https://doi.org/10.7569/JRM.2016.634128>
96. Yan L, Chou W, Jayaraman K (2014) Flax fibre and its composites—a review. *Compos Part B Eng* 56:296–317. <https://doi.org/10.1016/j.compositesb.2013.08.014>
97. Khan GA, Alam MS (2016) Surface chemical treatments of jute fiber for high value composite uses. *Res Rev J Mater Sci* 01(02):39–44. <https://doi.org/10.4172/2321-6212.1000110>
98. Suryanto H, Marsyahyo E, Irawan YS, Soenoko R (2014) Morphology, structure, and mechanical properties of natural cellulose fiber from mendong grass (*Fimbristylis globulosa*). *J Nat Fibers* 11(4):333–351. <https://doi.org/10.1080/15440478.2013.879087>
99. Reddy N, Yang Y (2007) Structure and properties of natural cellulose fibers obtained from sorghum leaves and stems. *J Agric Food Chem* 55(14):5569–5574. <https://doi.org/10.1021/jf0707379>
100. Vandenbrink JP, Hilten RN, Das KC, Paterson AH, Feltus FA (2012) Analysis of crystallinity index and hydrolysis rates in the bioenergy crop Sorghum bicolor. *Bioenergy Res* 5(2):387–397. <https://doi.org/10.1007/s12155-011-9146-2>
101. Cardoso CR, Oliveira TJ, Santana Junior JA, Ataíde CH (2013) Physical characterization of sweet sorghum bagasse, tobacco residue, soy hull and fiber sorghum bagasse particles: density, particle size and shape distributions. *Powder Technol* 245:105–114. <https://doi.org/10.1016/j.powtec.2013.04.029>
102. Sair S, Mansouri S, Tanane O, Abboud Y, El Bouari A (2019) Alfa fiber-polyurethane composite as a thermal and acoustic insulation material for building applications. *Appl Sci*. <https://doi.org/10.1007/s42452-019-0685-z>
103. Abdul Khalil HP et al (2012) Bamboo fibre reinforced biocomposites: a review. *Mater Des* 42:353–368. <https://doi.org/10.1016/j.matdes.2012.06.015>
104. Choi HY, Han SO, Lee JS (2009) The effects of morphological properties of henequen fiber irradiated by EB on the mechanical and thermal properties of henequen fiber/PP composites. *Compos Interfaces* 16(7–9):751–768. <https://doi.org/10.1163/092764409X12477436469871>
105. Di Giorgio L, Salgado PR, Dufresne A, Mauri AN (2020) Nanocelluloses from phormium (*Phormium tenax*) fibers. *Cellulose* 27(9):4975–4990. <https://doi.org/10.1007/s10570-020-03120-x>
106. Le TM, Pickering KL (2015) The potential of harakeke fibre as reinforcement in polymer matrix composites including modelling of long harakeke fibre composite strength. *Compos Part A Appl Sci Manuf* 76:44–53. <https://doi.org/10.1016/j.compositesa.2015.05.005>
107. Mwaikambo LY, Ansell MP (2001) The determination of porosity and cellulose content of plant fibers by density methods. *J Mater Sci Lett* 20(23):2095–2096. <https://doi.org/10.1023/A:1013703809964>
108. Mohanty AK, Misra M, Drzal LT (2005) *Natural fibers, biopolymers, and biocomposites*. CRC Press, Boca Raton, US
109. Herlina Sari N, Wardana IN, Irawan YS, Siswanto E (2018) Characterization of the chemical, physical, and mechanical properties of naoh-treated natural cellulosic fibers from corn husks. *J Nat Fibers* 15(4):545–558. <https://doi.org/10.1080/15440478.2017.1349707>
110. Reddy N, Yang Y (2005) Structure and properties of high quality natural cellulose fibers from cornstalks. *Polymer (Guildf)* 46(15):5494–5500. <https://doi.org/10.1016/j.polymer.2005.04.073>
111. Yu H, Liu R, Shen D, Wu Z, Huang Y (2008) Arrangement of cellulose microfibrils in the wheat straw cell wall. *Carbohydr Polym* 72(1):122–127. <https://doi.org/10.1016/j.carbpol.2007.07.035>
112. Liu M et al (2015) Effect of harvest time and field retting duration on the chemical composition, morphology and mechanical properties of hemp fibers. *Ind Crops Prod* 69:29–39. <https://doi.org/10.1016/j.indcrop.2015.02.010>
113. Park S, Baker JO, Himmel ME, Parilla PA, Johnson DK (2010) Cellulose crystallinity index: measurement techniques and their impact on interpreting cellulase performance. *Biotechnol Biofuels* 3:1–10. <https://doi.org/10.1186/1754-6834-3-10>
114. Charlet K, Jernot JP, Breard J, Gomina M (2010) Scattering of morphological and mechanical properties of flax fibres. *Ind Crops Prod* 32(3):220–224. <https://doi.org/10.1016/j.indcrop.2010.04.015>
115. Shah DU, Reynolds TP, Ramage MH (2017) The strength of plants: theory and experimental methods to measure the mechanical properties of stems. *J Exp Bot* 68(16):4497–4516. <https://doi.org/10.1093/jxb/erx245>
116. Andersons J, Spamiņš E, Joffe R, Wallström L (2005) Strength distribution of elementary flax fibres. *Compos Sci Technol* 65(3–4):693–702. <https://doi.org/10.1016/j.compscitech.2004.10.001>
117. Bourmaud A, Ausias G, Lebrun G, Tachon ML, Baley C (2013) Observation of the structure of a composite polypropylene/flax and damage mechanisms under stress. *Ind Crops Prod* 43(1):225–236. <https://doi.org/10.1016/j.indcrop.2012.07.030>
118. Silva FdA, Chawla N, Filho RDdT (2008) Tensile behavior of high performance natural (sisal) fibers. *Compos Sci Technol* 68(15–16):3438–3443. <https://doi.org/10.1016/j.compscitech.2008.10.001>
119. Zuccarello B, Militello C, Bongiorno F (2021) Influence of the anisotropy of sisal fibers on the mechanical properties of high performance unidirectional biocomposite lamina and micromechanical models. *Compos Part A Appl Sci Manuf* 143(Febuary):106320. <https://doi.org/10.1016/j.compositesa.2021.106320>



120. Summerscales J, Dissanayake NP, Virk AS, Hall W (2010) A review of bast fibres and their composites part 1—fibres as reinforcements. *Compos Part A Appl Sci Manuf* 41(10):1329–1335. <https://doi.org/10.1016/j.compositesa.2010.06.001>
121. Bourmaud A et al (2013) Relationships between microfibrillar angle, mechanical properties and biochemical composition of flax fibers. *Ind Crops Prod* 44:343–351. <https://doi.org/10.1016/j.indcrop.2012.11.031>
122. Yang Z, Peng H, Wang W, Liu T (2010) Crystallization behavior of poly( $\epsilon$ -caprolactone)/layered double hydroxide nanocomposites. *J Appl Polym Sci* 116(5):2658–2667. <https://doi.org/10.1002/app>
123. Zhang SY, Fei BH, Yu Y, Cheng HT, Wang CG (2013) Effect of the amount of lignin on tensile properties of single wood fibers. *For Sci Pract* 15(1):56–60. <https://doi.org/10.1007/s11632-013-0106-0>
124. Mura T (1987) *Micromechanics of defects in solids*, vol 3. Mechanics of elastic and inelastic solids, Springer, Dordrecht, Netherlands, Netherlands
125. Sevostianov I, Yilmaz N, Kushch V, Levin V (2005) Effective elastic properties of matrix composites with transversely-isotropic phases. *Int J Solids Struct* 42(2):455–476. <https://doi.org/10.1016/j.ijsolstr.2004.06.047>

**Publisher's Note** Springer Nature remains neutral with regard to jurisdictional claims in published maps and institutional affiliations.

